

USING A PATTERN RECOGNITION-BASED TECHNIQUE TO
ASSESS THE CONDITION OF SILICONE RUBBER
OUTDOOR INSULATORS

By

Ibrahim Marwan Jarrar

A Thesis Presented to the Faculty of the
American University of Sharjah
College of Engineering
in Partial Fulfillment
of the Requirements
for the Degree of

Master of Science in
Electrical Engineering

Sharjah, United Arab Emirates
May 2013

Approval Signatures

We, the undersigned, approve the Master's thesis of Ibrahim Marwan Jarrar.

Thesis Title: Using a Pattern Recognition-Based Technique to Assess the Condition of Silicone Rubber Outdoor Insulators

Signature

Date of Signature

(dd/mm/yyyy)

Dr. Khaled Assaleh
Professor, Department of Electrical Engineering
Thesis Advisor

Dr. Ayman El-Hag
Associate Professor, Department of Electrical Engineering
Thesis Co-Advisor

Dr. Aydin Yesildirek
Associate Professor, Department of Electrical Engineering
Thesis Committee Member

Dr. Mohammad Jaradat
Visiting Associate Professor, Department of Mechanical Engineering
Thesis Committee Member

Dr. Mohamed El Tarhuni
Head, Department of Electrical Engineering

Dr. Hany El Kadi
Associate Dean, College of Engineering

Dr. Leland Blank,
Interim Dean, College of Engineering

Dr. Khaled Assaleh
Director of Graduate Studies

ACKNOWLEDGEMENTS

First, my highest praise and thanks go to the almighty Allah, the lord of universe, who blessed me with the capability to complete this thesis successfully.

Moreover, no words can express the contribution of my parents and family, but I am greatly indebted to them for whatever I have achieved in my life. I am also deeply and profoundly thankful to my advisors Dr. Khaled Assaleh and Dr. Ayman El-Hag for supervising this thesis. Their sincere devotion and concern with my work was always a source of inspiration for me.

I would also like to express my deep sense of gratitude to all the professors in the electrical engineering department who worked hard to teach me the courses. I would also like to thank my managers and all my colleagues at Abu Dhabi Transmission and Dispatch Company (TRANSCO) for their continuous support and help during this period of time. I would also like to acknowledge the assistance of all other people who helped me to complete this work successfully.

DEDICATION

*To my father, may he rest in peace, my mentor and my beloved idol;
to my mother, the source of my inspiration, the guide to my success;
to all my beloved family, my priceless treasure,*

I dedicate this thesis to you all, and thank you for your sincere and precious support.

Abstract

Several transmission and distribution companies worldwide have started to replace their existing outdoor ceramic insulators with silicone rubber insulators. The use of silicone rubber insulators in outdoor insulators was first introduced in the market almost 30 years ago. Various studies have looked at the characteristics of this material under contaminated conditions. Despite the numerous advantages of silicone rubber insulators, they still suffer from several disadvantages, especially with the lack of sufficient and reliable tests from the manufacturers. The main disadvantage of silicone rubber insulators over ceramic ones is ageing. Ageing of silicone rubber insulators can occur due to arcing, partial discharge, weather conditions, and other factors. When silicone rubber insulators age with time, they may lose their hydrophobicity. Based on the water-filming resistance of these insulators, the hydrophobicity of their surface is manually classified into seven classes. The aim of this thesis is to develop an automatic system to classify and assess the condition of silicone rubber insulators using image processing and pattern recognition techniques. Accordingly, a database of images that represent the seven classes of surface hydrophobicity of silicone rubber will be created. In this thesis, several image processing techniques have been used to extract textural and statistical features. These methods include discrete cosine transformation, wavelet transformation, Radon transformation, contourlet transformation, and using a gray-level co-occurrence matrix. Stepwise regression was used as a dimensionality reduction technique and method of feature selection. Various classifiers were examined to evaluate the extracted features. The examined classifiers included linear, polynomial, k-nearest neighbor, and neural networks. A database of 358 gray-level 481x481 sized images was prepared to represent the seven hydrophobicity classes. An excellent recognition rate of 96.5% was achieved using fused features selected by a stepwise regression and classified by a neural network classifier. The 3.5% misclassified images were mainly due to confusions between adjacent classes that exhibited high levels of visual similarity. The system proposed by this thesis can be used to help utilities assess their silicone rubber insulators automatically and effectively.

Search Terms: Silicone Rubber, Hydrophobicity Classes, Database, Pattern Recognition, Image Processing, Neural Network, GLCM, Features Fusing, Stepwise Regression.

TABLE OF CONTENTS

CONTENTS

Abstract.....	6
List of Figures	10
List of Tables.....	12
CHAPTER 1: INTRODUCTION	13
1.1 Background	13
1.1.1 Overhead Transmission Lines (OHTL).....	13
1.1.2 Outdoor Insulators.....	13
1.1.3 Composite or Non-Ceramic Insulators (NCI).....	16
1.1.4 Ageing and Deterioration of NCIs	17
1.1.5 Deterioration Consequences	20
1.2 Literature Review	22
1.2.1 Online Monitoring Techniques	22
1.3 Thesis Objectives and Problem Formulation	29
CHAPTER 2: EXPERIMENTAL SETUP AND DATA COLLECTION	31
2.1 Samples Preparation.....	31
2.2 Preprocessing.....	34
2.3 Database Preparation and Description	37

CHAPTER 3: RESEARCH METHODOLOGY	40
3.1 Feature Extraction.....	40
3.1.1 Discrete Cosine Transform (DCT).....	41
3.1.2 Projections and Radon Transform	43
3.1.3 Wavelets Transform	46
3.1.4 Contourlet Transform.....	49
3.1.5 Gray Level Co-Occurrence Matrix (GLCM).....	50
3.2 Feature Selection	52
3.3 Pattern Recognition System	54
3.3.1 Linear Classifiers	55
3.3.2 Nonlinear Classifiers	56
3.3.2.1 Polynomial Classifier	56
3.3.2.2 K-Nearest Neighbor	57
3.3.2.3 Artificial Neural Network.....	58
CHAPTER 4: RESULTS AND DISCUSSION.....	61
4.1 Discrete Cosine Transform (DCT) Based Features	61
4.2 Radon Transform-Based Features	64
4.3 Wavelet Transform-Based Features.....	66
4.4 Contourlet Transform-Based Features	67
4.5 GLCM Based-Features	69
4.6 Feature Fusion	73

4.7 Results Discussion	75
CHAPTER 5: CONCLUSIONS AND FUTURE WORK:.....	78
REFERENCE LIST	80
VITA.....	83

List of Figures

Figure 1. Cap and Pin Ceramic Type Insulators [2].....	14
Figure 2. Long Rod Ceramic Type Insulators [2]	14
Figure 3. Various Types of Disc Insulators [4].....	15
Figure 4. Polymeric Insulator [4]	16
Figure 5. Ageing Process	18
Figure 6. Electric Field Distribution on Polluted Insulator Surface [10]	20
Figure 7. Chalking in NCIs [6]	21
Figure 8. Crazeing in NCIs [6]	21
Figure 9. Corona Cutting [6].....	22
Figure 10. Deterioration of Polymer Due to LC: (a). Tracking and (b). Erosion	22
Figure 11. Hot Spot Detected Using IR Camera [13]	23
Figure 12. Water Droplets from Hydrophobic to Hydrophilic Condition [6].....	26
Figure 13. Contact Angle(s) on Flat and Tilted Surfaces [16].....	27
Figure 14. HC 1 to HC 6 [16]	27
Figure 15. Samples of Class 1 to 3.....	31
Figure 16. Samples of Class 4 to 6.....	32
Figure 17. Class 7 Sample	32
Figure 18. HC1 to HC7 with Different % ABV Solutions	33
Figure 19. Experimental Setup Used in Acquiring Various HC Images	34
Figure 20. Image Preprocessing	37
Figure 21. Samples of the Obtained Grayscale Database of the 7 HCs	39
Figure 22. Proposed PR System.....	40
Figure 23. The Magnitude of the HC Images DCT	42

Figure 24. Zigzag Scanning Scheme [29].....	42
Figure 25. Zigzag Components of Class 5 DCT Image.....	43
Figure 26. Radon Transform Geometry [29]	44
Figure 27. Zero Angle Radon Transform of an HC1 Image	45
Figure 28. Zero Angle Radon Transform of an HC7 Image.....	45
Figure 29. Two Dimensional DWT Decomposition Process [26]	46
Figure 30. 1-Level Decomposition Using Haar Wavelet	47
Figure 31. 4-Level Decomposition Using Haar Wavelet	48
Figure 32. Contourlet Transform's Double Filter Bank Structure [26].....	50
Figure 33. Stepwise Regression Process.....	53
Figure 34. PR Structure	54
Figure 35. General Representation of a Classifier [34]	55
Figure 36. Second Order Polynomial Expansion of a 2-Dimensional Feature Space.	57
Figure 37. Structure of FF ANN	59

List of Tables

Table 1. Ceramic vs. Non-Ceramic Insulators [8].....	17
Table 2. Criteria of Evaluation HC [16]	28
Table 3. Database Summary	38
Table 4. Offset Values for the GLCM	51
Table 5. Description of the GLCM-Based Features.....	51
Table 6. Recognition Rates of the DCT Absolute Value FV	62
Table 7. DCT Magnitude and Phase FV Recognition Rates	63
Table 8. DCT Features' Recognition Rates with Stepwise Regression	64
Table 9. X-axis, Y-axis and Diagonal Projection Recognition Rates	65
Table 10. Radon Transform FV Comparison Results after Stepwise Regression	65
Table 11. Wavelet-Based Features' Recognition Rates	66
Table 12. Wavelet-Based Features' Classification Rates after Applying Stepwise Regression.....	67
Table 13. Wavelet vs Contourlet Statistical Features.....	68
Table 14. Wavelet vs. Contourlet Textural Features	69
Table 15. Comparison of Various GLCM Levels	70
Table 16. Comparison of Various GLCM Directional Angles	71
Table 17. Comparison of the Best GLCM Pixel Neighborhood Distance	72
Table 18. Feature Fusing with GLCM as a Base FV	74
Table 19. The Effect of DCT and Contourlet Features on the GLCM + Radon FV ...	75
Table 20. Confusion Matrix of One of the Round Robin Runs Using the ANN as a Classifier	77

CHAPTER 1: INTRODUCTION

1.1 Background

1.1.1 Overhead Transmission Lines (OHTL)

An electric power system can be divided into generation, transmission, and distribution networks. Transmission networks carry energy from generation to distribution networks with operating voltages higher than 33kV and often use overhead lines. For operating voltages less than 33kV, the distribution system substations interconnect and use both overhead lines and underground cables to deliver power to consumers. Overhead transmission lines transmit the majority of the electric energy in the power system and are preferable over the underground cables due to their lower cost, ease of installation, and inspection and fault localization. A high voltage transmission line typically consists of three phase conductors to carry the current and transport the power and energy, and one or two grounded shield conductors to protect the line from direct lightning strikes. The three-phase current-carrying lines are bare conductors, and therefore are insulated from the grounded supporting towers by outdoor insulators. These insulators can be either ceramic or non-ceramic insulators (NCI) [1].

1.1.2 Outdoor Insulators

Since the beginning of overhead transmission lines (OHTL) until around 30 years ago, the only insulators available for OHTLs were the ceramic insulators. These insulators came in two types: cap and pin, and long rod [2] (see Figures 1 and 2, respectively).

Ceramic insulators have gone through several improvements throughout the years in order to improve their mechanical strength, reliability, and long-term performance [3]. For example, several profiles were introduced to ceramic insulators to improve their contamination performance as shown in Figure 3 [4].



Figure 1. Cap and Pin Ceramic Type Insulators [2]



Figure 2. Long Rod Ceramic Type Insulators [2]

Despite these improvements, ceramic insulators still suffer from pollution and contamination problems which cause them to fail with time under severe arcing. Depending on the level of contamination, different insulators have different washing intervals which are hard to predict. Accordingly, manufacturers have suggested some anti-contamination methods that involve using [5]:

- Creepage extenders
- Semi-conductive glaze insulators

- Silicone grease coating (SGC)
- High voltage insulation coating (HVIC)

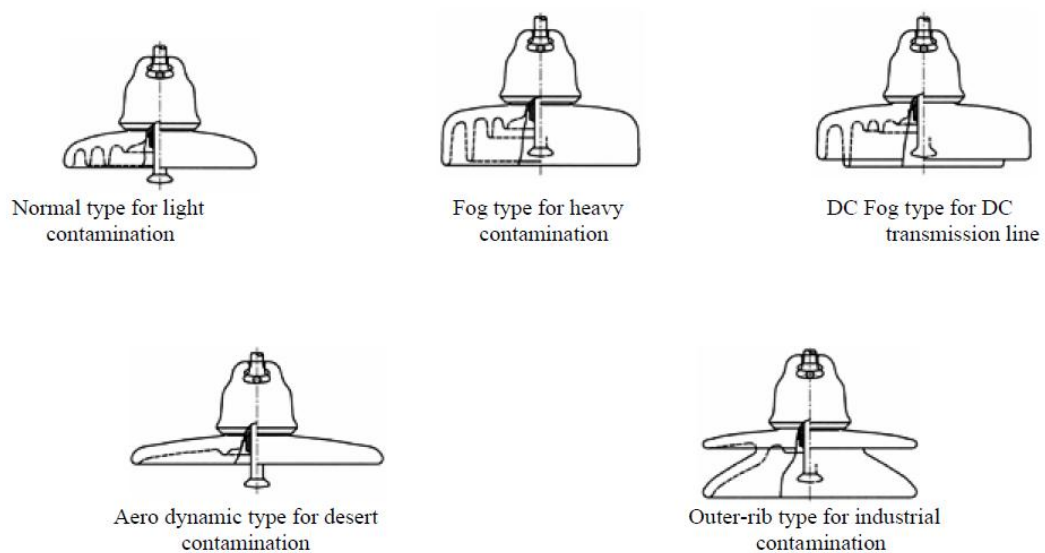


Figure 3. Various Types of Disc Insulators [4]

In spite of its effectiveness against contamination, creepage extender application is limited, expensive, and may cause an increase in partial discharge activities due to the electrical field distortion resulting from using different surface properties between the insulator and the extender. A semi-conductive glaze insulator is therefore a better solution to the contamination problem. Due to its semi-conductive properties, a semi-conductive glaze insulator allows little passage of current through its surface, which will limit the effect of dirt and fog accumulation and enhance the electrical field distribution along the insulator. On the other hand, the glaze will still increase the thermal runaway and the power loss due to its semi-conductive properties. Moreover, it is impractical to apply this technology on pre-existing insulators.

Using a silicone grease coating (SGC) is preferable to creepage extenders and semi-conductive glaze insulators. Applying SGC reduces the chances for flashover and excessive leakage currents. It also limits the effect of dirt and fog accumulation due to its water repellent nature. However, the application of SGC causes the contamination to stick and will require periodical removal and reapplication [6].

Alternatively, a high voltage insulator coating (HVIC) has also been used extensively in power systems. This coating has a better performance than SGCs in encapsulating contaminants, self-cleaning, hydrophobicity, and suppressing the leakage current. Despite their longer performance, HVICs still require a periodical removal and reapplication process, which is much more time consuming and labor intensive than the process needed for SGCs [5].

Due to their high failure rate and maintenance costs, ceramic insulators, in several countries, have been replaced by NCI insulators [2].

1.1.3 Composite or Non-Ceramic Insulators (NCI)

A typical modern composite insulator consists of a glass fiber-reinforced resin (GFR)-bonded rod onto which two metal end-fittings are attached. This GFR-bonded rod is covered with a polymeric rubber material (ethylene-propylene-diene monomer rubber [EPDM] or silicone rubber [SIR]), shaped like sheds [4]. Figure 4 displays a typical NCI.

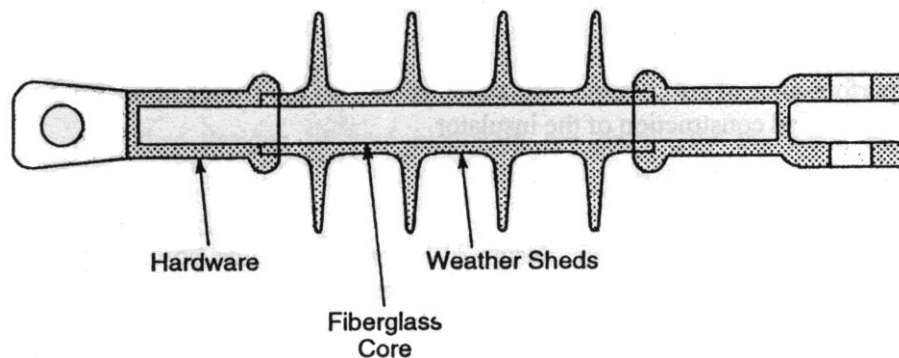


Figure 4. Polymeric Insulator [4]

Non-ceramic insulators outperform ceramic insulators because of their light weight, lower cost, and low surface energy which improves their outdoor performance due to their hydrophobic characteristics. However, several defects maybe present in the GFR or polymer material due to mishandling, ageing, or manufacturing defects

such as cracks, air voids, and impurities. Although most of the significant defects are detected in the commissioning stage, some defects are difficult to discover. Such undetected defects might grow and propagate with time under the continuous mechanical and electrical load. This can lead, along with ageing, to an increase in partial discharge (PD) activities, loss of hydrophobicity, leakage current (LC), and sometimes flashover [3]. Also, NCIs suffer from a number of drawbacks such as ageing and unknown long-time reliability [7]. Table 1 provides a comparison between ceramic and non-ceramic insulators [8].

Table 1. Ceramic vs. Non-Ceramic Insulators [8]

	FACTORS	CERAMIC	NON-CERAMIC
1	Resistance to flashover in polluted atmosphere.	Low	High
2	Contamination and pollution	Highly affected	Performance not affected
3	Hydrophobicity	Not hydrophobic	Unique hydrophobic character.
4	Self-cleaning property	Due to glaze and inclination of sheds.	Due to hydrophobicity recovery properties
5	Maintenance	Needs maintenance like cleaning, washing, greasing.	No maintenance is Normally required
6	Weight	Heavy	10% to 35% of ceramic insulator
7	Resistance to breakage and vandalism	Breakable in vandalism-prone areas	Unbreakable

1.1.4 Ageing and Deterioration of NCIs

One of the main factors that leads to non-ceramic insulator failure is ageing. Ageing occurs in NCIs and coated insulators due to their organic nature. Ageing of NCIs causes a decrease in surface resistance which causes the insulator surface to become more prone to contamination accumulation and water filming [9]. Two main factors significantly accelerate the ageing process. The first one is electrical stresses

such as leakage current and corona. These stresses usually happen after the formation of dry bands, increases in the pollution or humidity level, or due to overvoltage stresses. The second type of stress is environmental such as heat, ultraviolet light (UV), acid, wind, rain, snow, salts, and biological degradation [7]. Electrical and environmental stresses can lead either to loss of low molecular weight components or de-polymerization as in chain scission or oxidation. These changes result in loss of elasticity, erosion, roughness, chalking, cracking, and loss of hydrophobicity which in turn leads to the loss of electrical and mechanical strength of the NCI (see Figure 5) [9]. Moreover, contamination and moisture on the insulators causes electrical stresses on the NCI such as partial discharge and leakage current. This causes a loss of hydrophobicity and degradation of the polymer material.

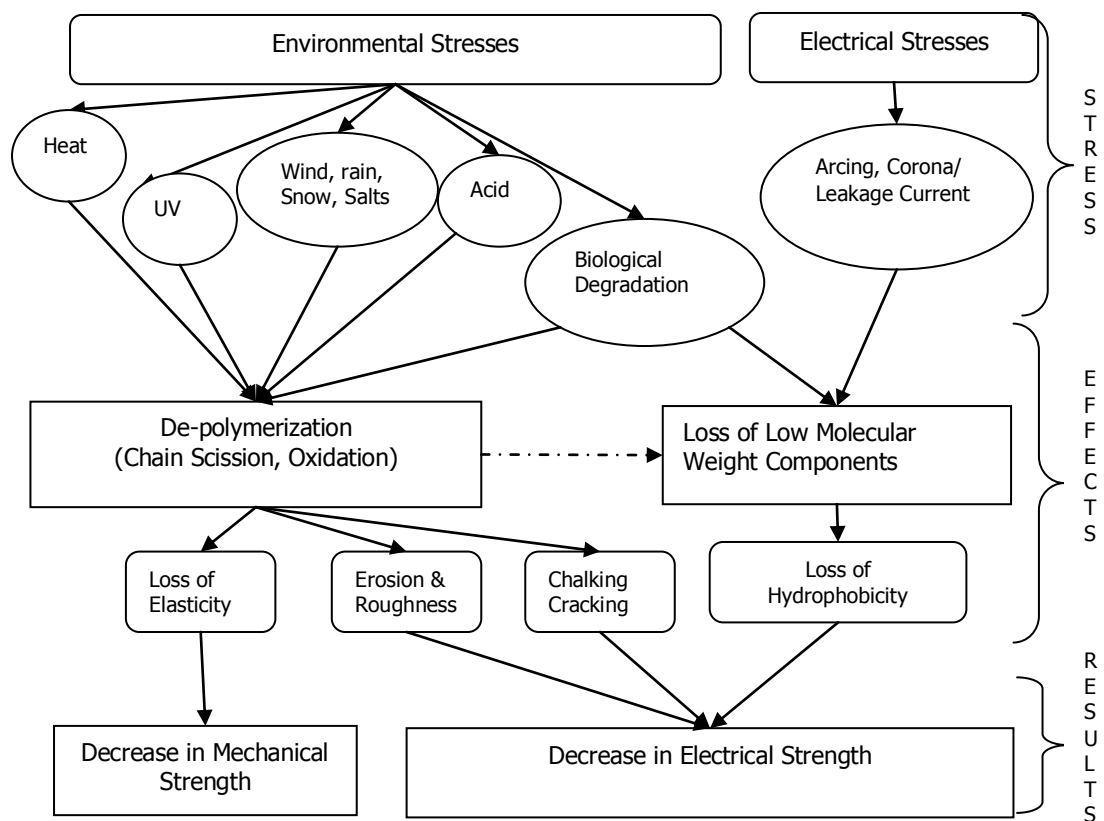


Figure 5. Ageing Process

- Leakage Current (LC):

Hydrophobic insulators have a very low surface tension and therefore a high surface resistance, which is important in limiting the leakage current. This gives the insulator the ability to repel water and hence prevent the formation of water filming (as opposed to ceramic insulators). With the aid of humidity, fog, dew, or rain, conductive contamination forms conductive wetted areas on the insulator surface [7]. This conductive path triggers surface discharges which reduce the surface energy of the NCI. This enhances the formation of water filming which could lead to a leakage current and dry band arcing. Usually environmental and electrical stresses will cause localized loss of hydrophobicity which will lead to the formation of various surface resistances and hence different levels of current density. Leakage current will be higher on the areas of less surface resistance, causing heat to develop in those layers which will accelerate the ageing of the insulator and the formation of dry bands as a result of the water evaporation [9]. A voltage difference will develop across those bands promoting what is known as dry band arcing. The energy dissipated from the dry band arcing could raise the temperature of these spots up to 500°C or more. This thermal energy will greatly accelerate loss of low molecular weight components and thus deterioration and ageing of the insulator [6].

- Partial Discharge (PD):

Another form of electrical stress is the partial discharge which is the result of electric field enhancement due to the availability of water droplets on the insulator surface (see Figure 6). This enhancement is due to the different permittivity of the layers of interface: water ($\epsilon=80$), insulator ($\epsilon= 2-3$), and air ($\epsilon=1$) [10]. If this electrical field exceeds the breakdown voltage of air (22 kV/cm), partial discharge will be initiated [5]. The energy dissipated from the repeated discharges causes damages to the surface of the insulator promoting temporary loss of hydrophobicity in those areas. Usually corona and UV radiations cause temporary loss of hydrophobicity due to de-polymerization as a result of the chain scission or oxidation reactions. Once these environmental and electrical stresses disappear, the SIR regains, partially or fully, its hydrophobic properties [11]. Continuous stresses on the insulator surface can lead to a complete deterioration and loss of hydrophobicity of the SIR. Chain scission or oxidations that accompany PD can cause the formation of acidic

byproduct and loss of low molecular weight components. These effects initiate chemical reactions, and cause the polymeric matrix bonds to break, hence forming silanol groups, cyclic silicone oligomers, and intermolecular forces. These intermolecular forces will restrain the cyclic silicone oligomers from roaming back to the surface. This will in turn curb the loss of the recovery property of the SIR [9].

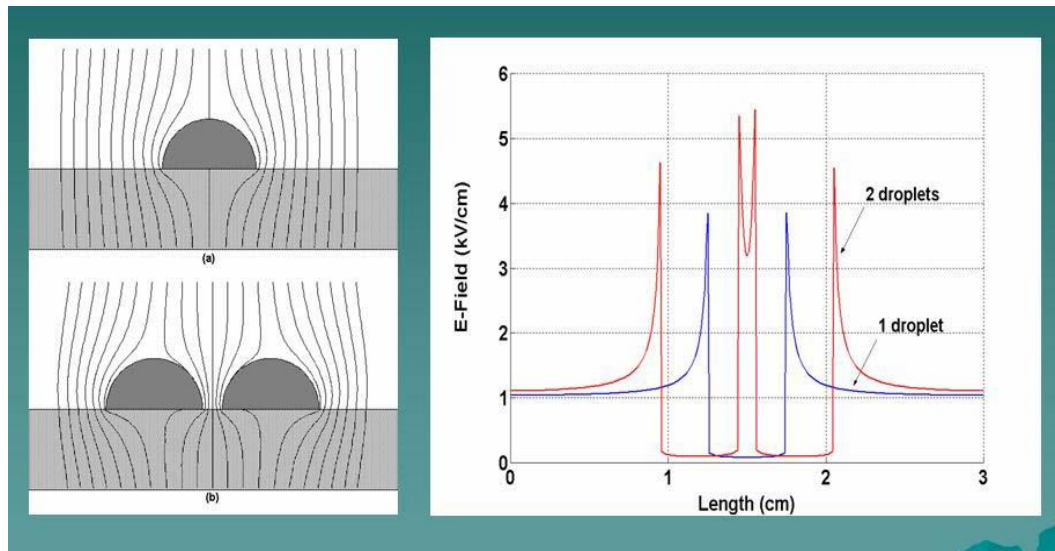


Figure 6. Electric Field Distribution on Polluted Insulator Surface [10]

1.1.5 Deterioration Consequences

Due to the electrical and environmental stresses, the insulator will deteriorate. Deterioration of the insulator can appear in several forms such as loss of gloss and color, loss of hydrophobicity, chalking, crazing, alligating, corona cutting, punctures, tracking, and erosion [11]. Usually the first and common signs of ageing are discoloration and loss of hydrophobicity. Then depending on the reason and factors of ageing, various forms of deterioration can develop. UV radiation and electrical activities on the surface of the NCI usually gives a toothed and whitish dusty appearance to the insulators (this is known as chalking) [6] as shown in Figure 7. Chalked insulators allow for more absorption of water and contamination, which accelerates the ageing process. Electrical stresses such as PD and arcing cause cracks in the surface of the insulators. If these cracks are less than 0.1 mm deep, they are called crazing [9] as shown in Figure 8 [6]. A more severe state of crazing where the depth of the cracks is more than 0.1 mm is called alligating, and could lead to the

exposure of the rod. Also, as was discussed in the previous section, persistent corona, especially in the end fittings or due to improper bonding between the housing and rod could lead to a condition known as corona cutting which exposes the insulator to severe electrical and chemical degradation [6], as shown in Figure 9. Due to the organic nature of the polymeric materials, leakage current can cause permanent tracking and erosion of the polymeric material [7]. Tracking is more serious than erosion since it forms carbonized conducting paths on the surface of the insulator, while erosion is non-conductive and is a slower form of degradation (see Figure 10) [6].

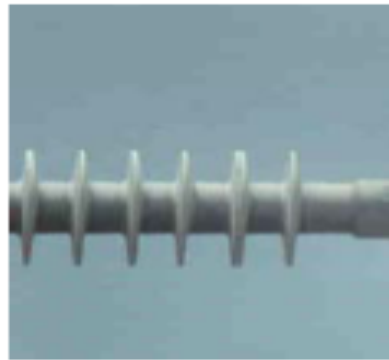


Figure 7. Chalking in NCIs [6]



Figure 8. Crazeing in NCIs [6]



Figure 9. Corona Cutting [6]

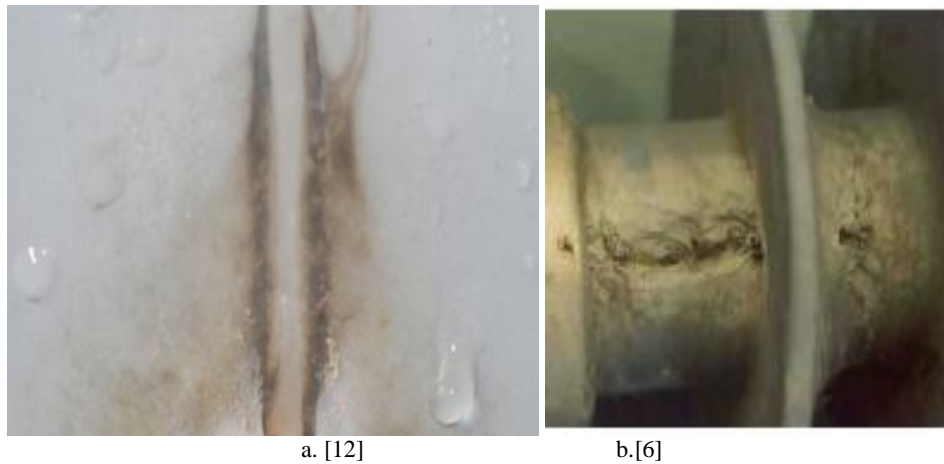


Figure 10. Deterioration of Polymer Due to LC: (a). Tracking and (b). Erosion

1.2 Literature Review

1.2.1 Online Monitoring Techniques

Due to the importance of monitoring insulators condition, many utilities around the globe have adopted several effective methods to evaluate insulators' surface conditions. Most of these techniques depend on the observation of LC and PD activities like infrared (IR) cameras, image intensifiers and current transformers (CT). Other techniques, such as contact angle measurements and hydrophobicity evaluation techniques, are used to monitor the quality and the level of ageing in the rubbery material [2]. In the following lines, a brief description of each technique will be given.

- IR camera:

This technique detects the heat distribution around the rubber housing and end fitting area. Places with high corona activities and increasing LC activities appear as

hot spots in the IR camera due to the heat emission resulting from the losses (see Figure 11) [13].

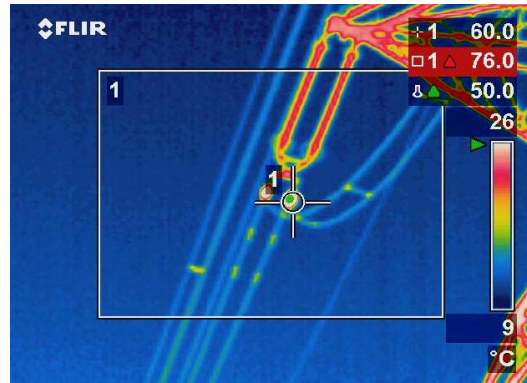


Figure 11. Hot Spot Detected Using IR Camera [13]

Using this technique, problems such as end-fitting rusting, loose or missing grading rings, punctures in the rubber housing, and poor conditions of end fitting seals can be determined [3]. Although using an IR camera can help specify the location of the most degraded areas, it doesn't assess the level of deterioration of the polymeric material. There is still no correlation between the level of ageing in the insulator and the thermal coloring due to the availability of several sources of heat emission around the insulator.

- **Optical Detection (Light Intensifier and UV Camera):**

Another measurement possibility is to detect partial discharge activities optically. Directly after the occurrence of PD, a radiation of light in the ultraviolet, visible, and infrared areas is emitted. Around 90% of the total energy in this discharge spectrum is emitted in the ultraviolet area between 250 and 400 nanometers [14]. This phenomenon can be used for optical detection of PD. The spectrum depends on the surrounding medium and must be considered by the selection of the optical detection system. Night vision and low-light enhancers as well as fiber-optic cables, are used depending on the spectral region. Recently, daytime intensifiers have also been used to detect PD activities. Optical detection is an excellent method to detect PD activities around the outdoor insulator. Also, localization of the defect is possible. However, optical detection does not reveal any information about the condition of the insulator,

especially if there is no corona in the vicinity of the insulator. Moreover, it can be used to detect instant PD activities only, with no information about LC. It also cannot be used to measure the quantity of PD since calibration is not possible [2].

- Current Transformer (CT):

Two types of CTs can be used to detect PDs and LC. A high frequency CT (HFCT) is used to detect PDs while normal CTs are used to monitor LC. Both types of CTs can be mounted on the ground conductor of the OHTL. Very narrow electrical pulses of current will travel along the grounding conductor to the earth when a PD occurs. This signal can be detected using an HFCT. On the other hand, first and third harmonics dominate in the occurrence of LC, and hence 50/60 Hz CT will be sufficient to sense the LC. Using CTs has several advantages as it is a non-intrusive test and can be performed online without disconnecting the insulator from the system [15]. Moreover, the measuring system can be portable if a clamp CT is used. The disadvantages of using CTs include poor directionality, low signal-to-noise ratio (SNR), and the necessity to have access to ground cables. Using CTs or HFCTs, the level of PD or LC can be correlated but the source and the location remain unknown. In addition, the PD and LC detected could be due to other reasons besides the condition of the insulator [14].

- RF Antenna:

RF antenna detection captures RF energy generated by a PD. Analysis of the intensity of the radiation, shape of the pulse, and location of the discharge relative to the AC cycle of the device reveals a lot of information about the type of fault and the severity of the insulation damage [14]. The detection system is also capable of performing a frequency sweep, detecting the position of the signal, and acquiring a time domain waveform of the RF signal. The RF signals associated with corona discharges usually lie in the 20 MHz - 30 MHz range. Discharges because of voids and floating components may lie elsewhere in the spectrum. An RF signal analyzer can be easily tuned to different frequencies, depending on the type of discharge being analyzed [15]. Although the RF technique is safe, non-intrusive, and can be used to determine the location of the PD, it still suffers from several disadvantages. These include capturing RF noise, high attenuation, and the high cost associated with the measuring instrumentation.

- **Acoustic Emission Technique:**

Each partial discharge delivers acoustic energy that can be detected as sound. The propagation speed of the acoustic wave depends on the surrounding medium. Reflections, refraction, and absorption influence the sound propagation, which must be considered during detection and interpretation. Microphone transducers can be used as sensors. The acoustic emission technique deals with much lower frequency than the RF method. This method has several advantages including ease of inspection, relatively low cost, and the fact that no connection to the insulator is needed [14]. On the other hand, the need for pre-amplifiers, lack of information about leakage current, and difficulty of assessing the conditions of the insulators' surface are some of the disadvantages of using the acoustic emission inspection technique.

- **Visual Inspection:**

The most common way of monitoring insulators condition is visual inspection. Since most of the first signs of deterioration can be noticed visually or with the aid of some detecting devices, utilities all around the world are still sending patrolling teams or helicopter tours to inspect the condition of the insulators [2]. These patrolling teams are equipped with different tools to help them assess the condition of the insulators such as IR cameras, or any other diagnostic tool previously mentioned. Patrolling tours can be divided into two types: day patrolling and night patrolling. They are also divided into two categories based on the level of inspection: general patrolling and tower-to-tower patrolling. Although these inspections are thorough and informative, they consume a lot of time and manpower and they become impractical for long and far away lines. Utilities and maintenance companies worldwide are suffering from the continuous increase of inspection costs and they are in a constant search for an alternative monitoring and evaluation methods.

- **Hydrophobicity Evaluation:**

Deterioration of the polymeric material is always accompanied with loss of its hydrophobicity. As discussed before, hydrophobicity of the material is its ability to repel and resist water flow on its surface. When the surface of the insulator is hydrophobic, water droplets will not flow on the surface and will form independent small droplets with contact angles ($>90^\circ$). When the surface of the insulator experiences ageing, this contact angle starts to decrease until the surface is completely

hydrophilic and the water droplets transfer to water films. The change of the hydrophobicity is depicted in Figure 12 [6].

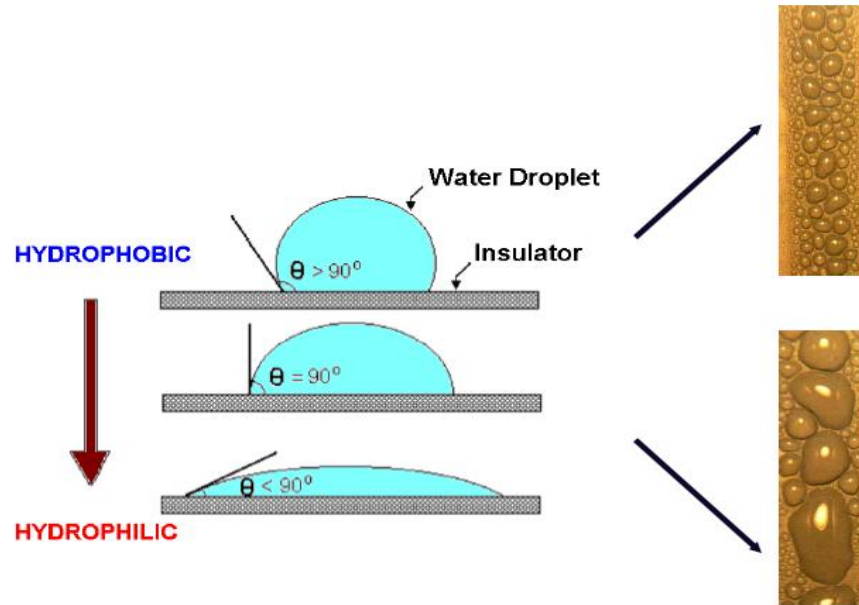


Figure 12. Water Droplets from Hydrophobic to Hydrophilic Condition [6]

One of the techniques to measure hydrophobicity or the hydrophobicity class (HC) of NCIs is by measuring the contact angle. In this technique, water droplets are injected with a syringe and the contact angle (θ) of the droplet is measured on a flat surface. On the other hand, the difference between the advancing (θ_a) and receding angle (θ_r) is measured when the surface is tilted as shown in Figure 13 [16]. This method is only applicable in a laboratory environment and cannot be applied to field conditions.

Another well-known measurement technique is by spraying a fine water mist on NCI insulators. Then, the surface can be classified from HC 1 (completely hydrophobic) to HC 7 (completely hydrophilic) as shown in Figure 14 [16].

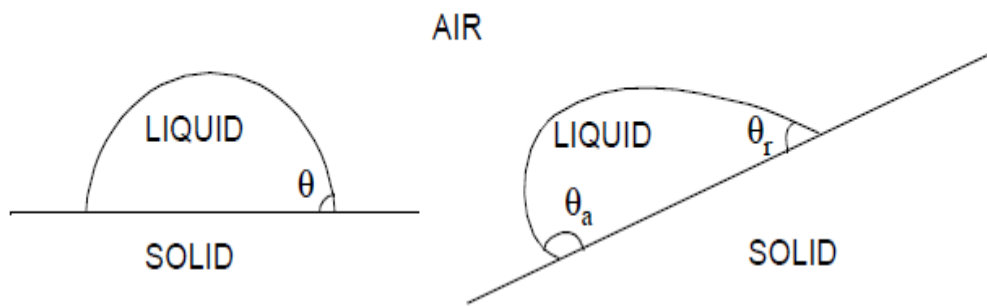


Figure 13. Contact Angle(s) on Flat and Tilted Surfaces [16]

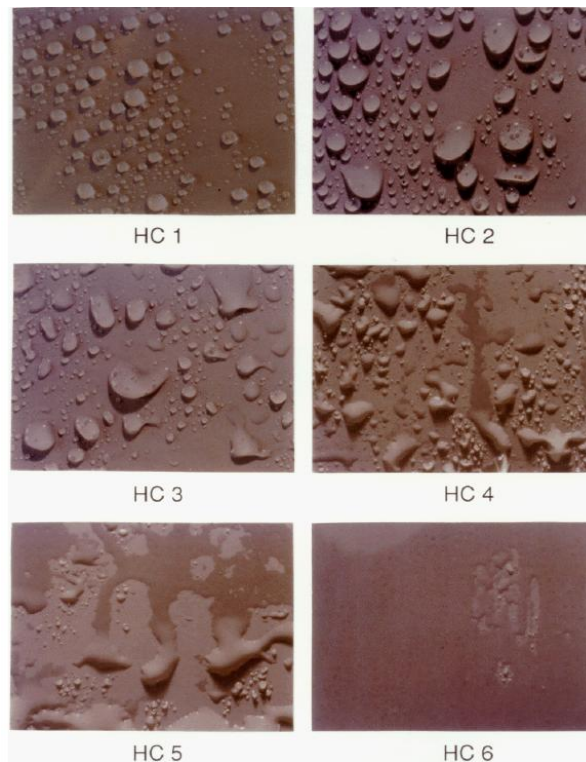


Figure 14. HC 1 to HC 6 [16]

The classes are determined based on the contact angle of the droplets and the size of the wetted area according to the criteria shown in Table 2 [16]. This method is called the STRI hydrophobicity classification, and it is a comprehensive evaluation of the ageing condition of the insulator. The main issue with this method is that it totally depends on human judgment.

Table 2. Criteria of Evaluation HC [16]

HC	Description
1	Only discrete droplets are formed. $\theta = 80^\circ$ or larger for the majority of droplets.
2	Only discrete droplets are formed. $50^\circ < \theta < 80^\circ$ for the majority of droplets.
3	Only discrete droplets are formed. $20^\circ < \theta < 50^\circ$ for the majority of droplets. Usually they are no longer circular.
4	Both discrete droplets and wetted traces from the water runnels are observed. Completely wetted areas $< 2 \text{ cm}^2$. Together they cover $< 90\%$ of the tested area.
5	Some completely wetted areas $> 2 \text{ cm}^2$, which cover $< 90\%$ of the tested area.
6	Wetted areas cover $> 90\%$; i.e., small un-wetted areas (spots/traces) are still observed.
7	Continuous water film over the whole tested area.

- Image Processing:

To overcome the subjectivity of human judgment, several researchers have suggested the use of digital image processing (DIP) to analyze and measure the contact angle and hence determine the HC and evaluate the condition of the insulator. In [17] the researchers used DIP to calculate and evaluate the hydrophobicity of polymeric insulators. The suggested method utilizes human interference in specifying the region of testing and marking the area that contains the water droplets by extracting unrelated images' backgrounds. The classification depends on the ratio of the area of the maximal water droplet or water trace divided by the area of the whole image. It also considers the shape coefficient of the maximal water droplet or water trace to measure the HC. Although this method is effective in online measurement of the insulator condition, it still depends on the interference of the operator in specifying the region of the image and removing the selected area's background. Also, the accuracy of the technique is subjected to the operator's skills while taking the pictures and the distance from which the picture is taken. The issue of human

intervention is solved in [18] by creating an image processing algorithm that is based on extracting water droplets' images from the background, fitting the water droplets' contours using the orthogonal polynomial, and measuring the contact angle to estimate the insulator's hydrophobicity. The main issue with this method is that it doesn't apply to practical cases or to online evaluation of the insulator. The researchers assume a fixed rotation of 15° for the water droplets and consider the droplet to be in the middle of the insulator, which is not always the case. Also, the technique is based on a single droplet to evaluate the insulator rather than the practical case of several droplets of various sizes. In general, this method is applicable to certain and specific conditions and cannot be used to evaluate insulators in general. It is also a localized evaluation of the surface where the droplet resides and can't be generalized to judge the whole insulator surface conditions.

Several other researchers have used DIP to evaluate the HC of insulators [19-22]. Different techniques were implemented including circular factor, Hough transformation, segmentation, scaled entropy, histogram analyses, surface energy, textural analysis, and fractal dimension. While some researchers failed to characterize a clear association with the HC, others were successful in creating a mathematical relationship to the HC of the insulator. However, none of them were able to generalize a classifier. Recently, the authors of [23] and [24] have combined more than one feature such as area and shape in order to overcome the shortage of utilizing a single feature. Utilizing several features to evaluate the condition of the insulator has eliminated the high error risk of making a single decision, poor reliability, and fault tolerance due to single-feature evaluation. Although these methods have enhanced the recognition rate, they are still not ideal for evaluating the insulator in variable conditions. Their success depends on a specific arrangement of fixed distance, light level, and insulator position and shape. Any alteration of the experiment conditions would require a reconfiguration of the decision tree boundaries to correctly classify the insulator.

1.3 Thesis Objectives and Problem Formulation

As discussed in the introduction and the literature review, there is currently no comprehensive online method to assess the class and condition of NCIs. Most of the online techniques focus on PD and LC detection, but with no direct correlation with

the condition of the NCI. The best direct method that correlates the condition and level of deterioration of the NCI is the hydrophobicity measurement. Currently, the implemented hydrophobicity measurement is done manually and depends on subjective human judgment as suggested by the STRI guide [16]. The attempts to develop an automatic online system based on image processing were limited by various factors including human intervention, localized evaluation, or specific conditions. The objective of this thesis is to develop an online monitoring system to assess the condition of silicone rubber (SIR) insulators without the intervention of an operator. The developed system will be based on various digital image processing (DIP) algorithms to extract distinguishing features. After the feature extraction, selection, and formation of the feature vector, methods of pattern recognition (PR) will be utilized to classify the images and hence the class of the insulator. Being learning-based, the proposed system can be trained to learn various conditions of the SIR training samples. In addition to developing an automatic system to assess the condition of the SIR insulators into seven HC classes with a high recognition rate while overcoming the issues of human subjectivity, variable conditions, and localized evaluation, this thesis aims to achieve the following objectives:

- The preparation of an images database for the seven hydrophobicity classes. Such a database does not currently exist.
- The evaluation and documentation of various statistical and textural features extracted using several DIP techniques, such as discrete cosine transform (DCT), wavelet transform, projection or Radon transform, gray level co-occurrence matrix (GLCM), and contourlet transform.
- The evaluation and comparison of the performance of various classification techniques including linear, polynomial, k-nearest neighbor (KNN), and artificial neural network (ANN).

CHAPTER 2: EXPERIMENTAL SETUP AND DATA COLLECTION

2.1 Samples Preparation

Samples used in this study were prepared using 10cm x 10cm ceramic tiles. The ceramic tiles were coated with a room-temperature-vulcanizing (RTV) silicone rubber coating. To achieve different hydrophobicity classes (HC), from class 1 to class 7 according to Table 2, these coated tiles were aged by dipping them into tap water for several days and monitoring their condition. Using this method, samples of classes 1 to 3 were prepared (see Figure 15).

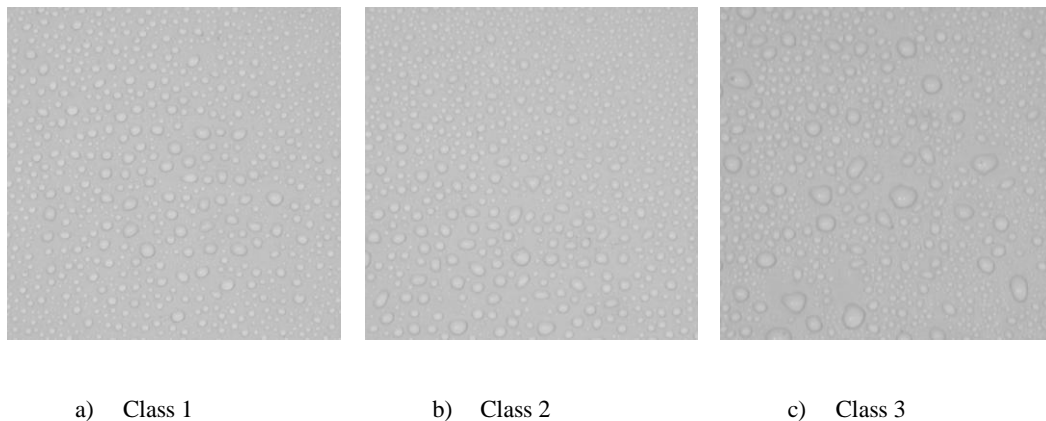


Figure 15. Samples of Class 1 to 3

To prepare the other classes, they were aged using electrical stresses such as partial discharge (PD). A high voltage of 5 kV was applied through several sharp electrodes positioned above the coated tiles. This is because the enhanced electric field on the tip of the sharp electrode triggers the occurrence of PDs which accelerates the ageing process. Figure 16 demonstrates classes 4 to 6, respectively. Finally, class 7, a totally hydrophilic surface, was prepared by using sand paper to damage the surface hydrophobicity as depicted in Figure 17.

The previous methods of ageing to obtain the seven classes suffer from several drawbacks. First, they still depend on the human judgment to determine the classes after ageing. Also, there is no clear relation between the time required to immerse a

sample in the water and the degree of hydrophobicity degradation. Moreover, the above-mentioned methods cause inconsistencies in the outcome of the ageing process due to the hydrophobicity recovery property of SIR. So, it is important to use a more consistent method in creating various HCs.

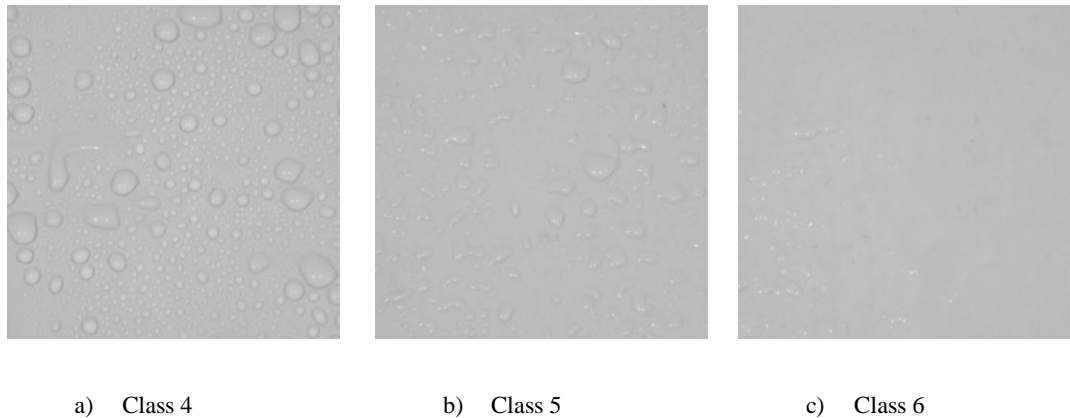


Figure 16. Samples of Class 4 to 6

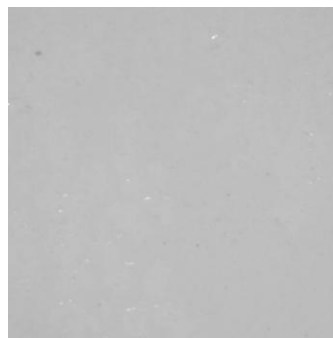


Figure 17. Class 7 Sample

Using the method suggested by [21], images of classes 1 to 7 were obtained. The method suggests the use of distilled water and alcohol solutions to spray the coated samples. Alcohol solutions have lower surface tension reactions to coated surfaces, which makes the sprayed droplets react as if the surface is actually aged.

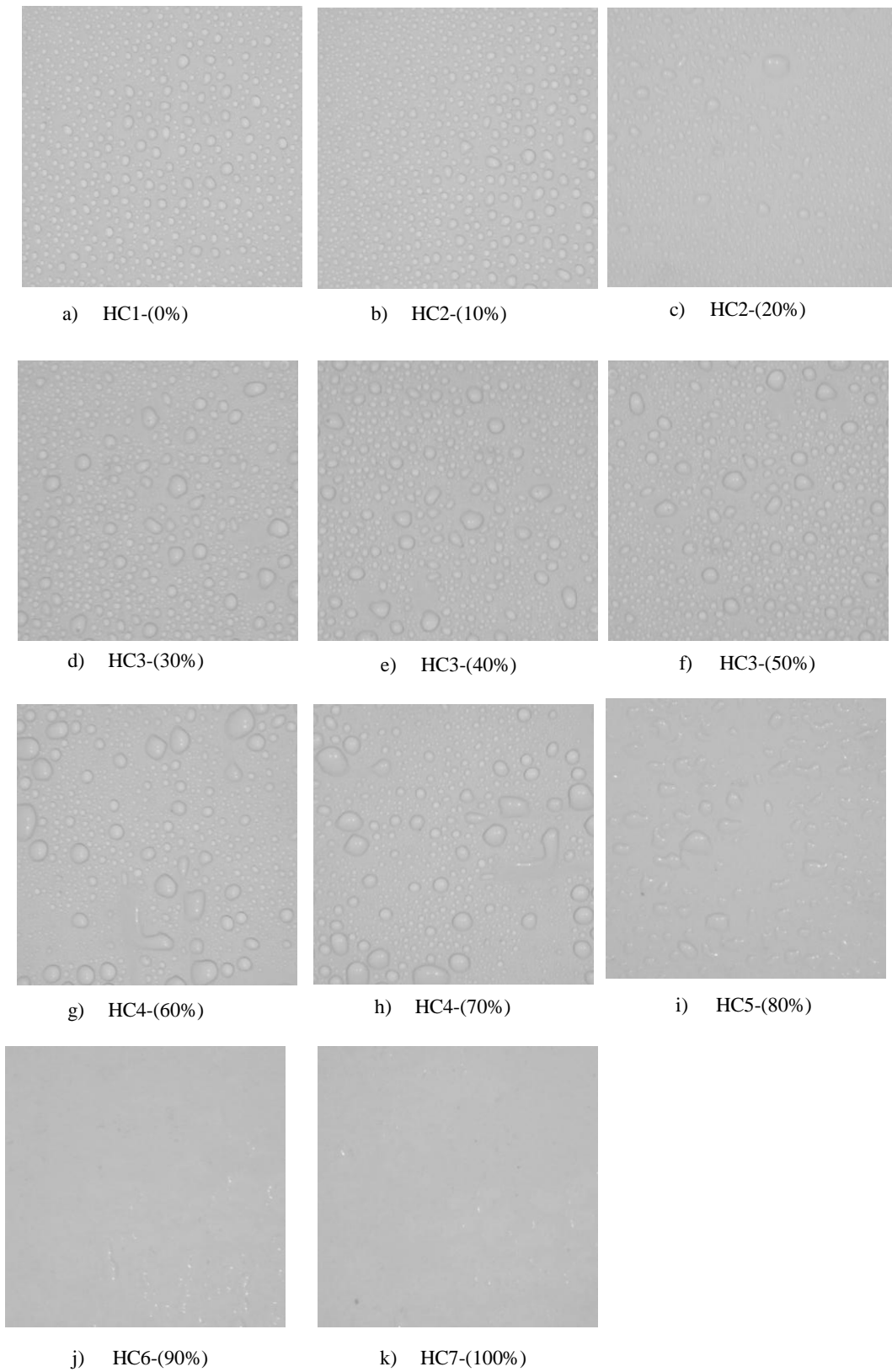


Figure 18. HC1 to HC7 with Different % ABV Solutions

Depending on the percentage of alcohol by volume (ABV) in the spraying solution, various HC classes can be obtained from class 1 with 0% ABV to class 7 with 100% ABV. Figure 18 demonstrates the obtained HC images, using different ABV percentages. A similar experimental setup is imitated in this research for the purpose of acquiring the HC images as suggested in [25] and demonstrated in Figure 19. Spraying the solution mist can be done through a common spray bottle, or an automatic spraying system can be designed in a later stage as a part of an automated outdoor insulator inspection system as proposed in [25].

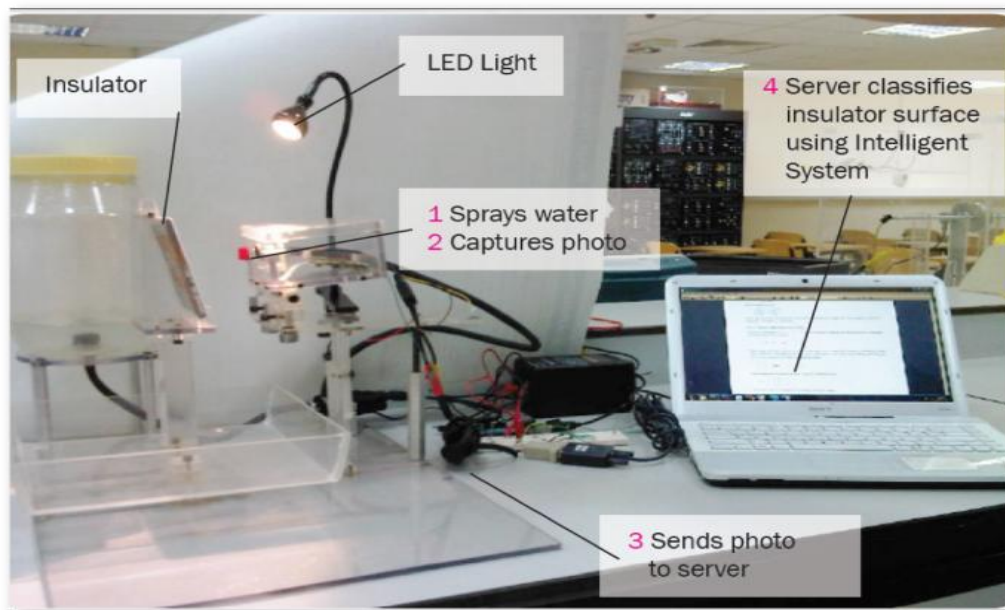


Figure 19. Experimental Setup Used in Acquiring Various HC Images

2.2 Preprocessing

In order to prepare a unified image database and data matrices from which the features will be extracted, MATLAB[®] R2011b was used to read, acquire, and apply common preprocessing schemes on all obtained images. This process will enhance the feature extraction step and the performance of the digital image processing (DIP) and pattern recognition (PR) algorithms. A brief introduction of DIP along with some of the relevant techniques used in this research will be described.

An image is basically a two-dimensional function, $f(x, y)$, where x and y are the spatial or plane coordinates. The value of f at any (x, y) denotes the intensity or gray level of the image at that point [26]. In other words, an image is a 2-D light-intensity function bounded by the following inequality [27]:

$$(black)0 \leq f(x, y) \leq f_{max}(white) \quad (1)$$

The lower limit indicates that the intensity is a real positive quantity while the upper limit theoretically can be infinity but in real practical systems, it is restricted by the physical imaging capability to present the intensity level of an image. When the values of the coordinate and the amplitude of the image are finite and discrete, this image is called a digital image (DI). DIs are considered matrices whose elements are the pixel values of the image. DIs in MATLAB are of several types [28]:

- Grayscale image, where the values of the pixels indicate the grey scale and are presented in a single $m \times n$ matrix.
- Binary image, which presents the image as black (0) and white (1) based on a threshold. The threshold can be calculated or preset using built-in functions.
- Intensity image, a single matrix where the pixels represent intensities within some range.
- RGB image or a true color image, which represents an m -by- n -by-3 data array (rows \times columns \times 3) that defines red, green, and blue color components for each individual pixel.
- Indexed image, which consists of 2 matrices: color-map and index. The numbers in the first matrix are an instruction of what number to use in the color-map.

Converting an image between the mentioned types is possible in MATLAB and operations such as image arithmetic (adding, subtracting, multiplying, and dividing) and spatial transformation (resizing, rotation, and cropping) are possible. Moreover, image enhancement such as filtering, which includes smoothing, sharpening, edge enhancement, and de-blurring, can also be achieved. Filtering in 2D space can be done either in the spatial dimension or the frequency domain. De-blurring can be done by means of filtering. Blurred images can be modeled as in Equation 2

$$B = Df + n \quad (2)$$

where B is the blurred image, D is the distortion operator, f is the image, and n is additive noise.

Some of the common techniques used in de-blurring are [27], [29]:

- Wiener filter: This method can be used when the frequency characteristics of the image and additive noise are known.
- Regularized filter: Can be used when limited information is known about the additive noise.
- Lucy-Richardson algorithm: This algorithm presumes Poisson noise statistics and prioritizes the likelihood that the resulting image is an occasion of the blurred image.
- Blind de-convolution algorithm: This algorithm works similarly to the accelerated, damped Lucy-Richardson algorithm, but with better performance when no information about the distortion (blurring and noise) is known.

A series of preprocessing steps were performed on the obtained images as demonstrated in Figure 20. The original RGB image was downsized by a factor of 4 to reduce its size to 804×1072 . This is done for more effective storage and computational complexity of the system since the high resolution of the acquired image is unnecessary for the application at hand. Further size reductions can be done by cropping a square segment of size 480×480 from the center of the image to remove any unneeded background objects in the image.

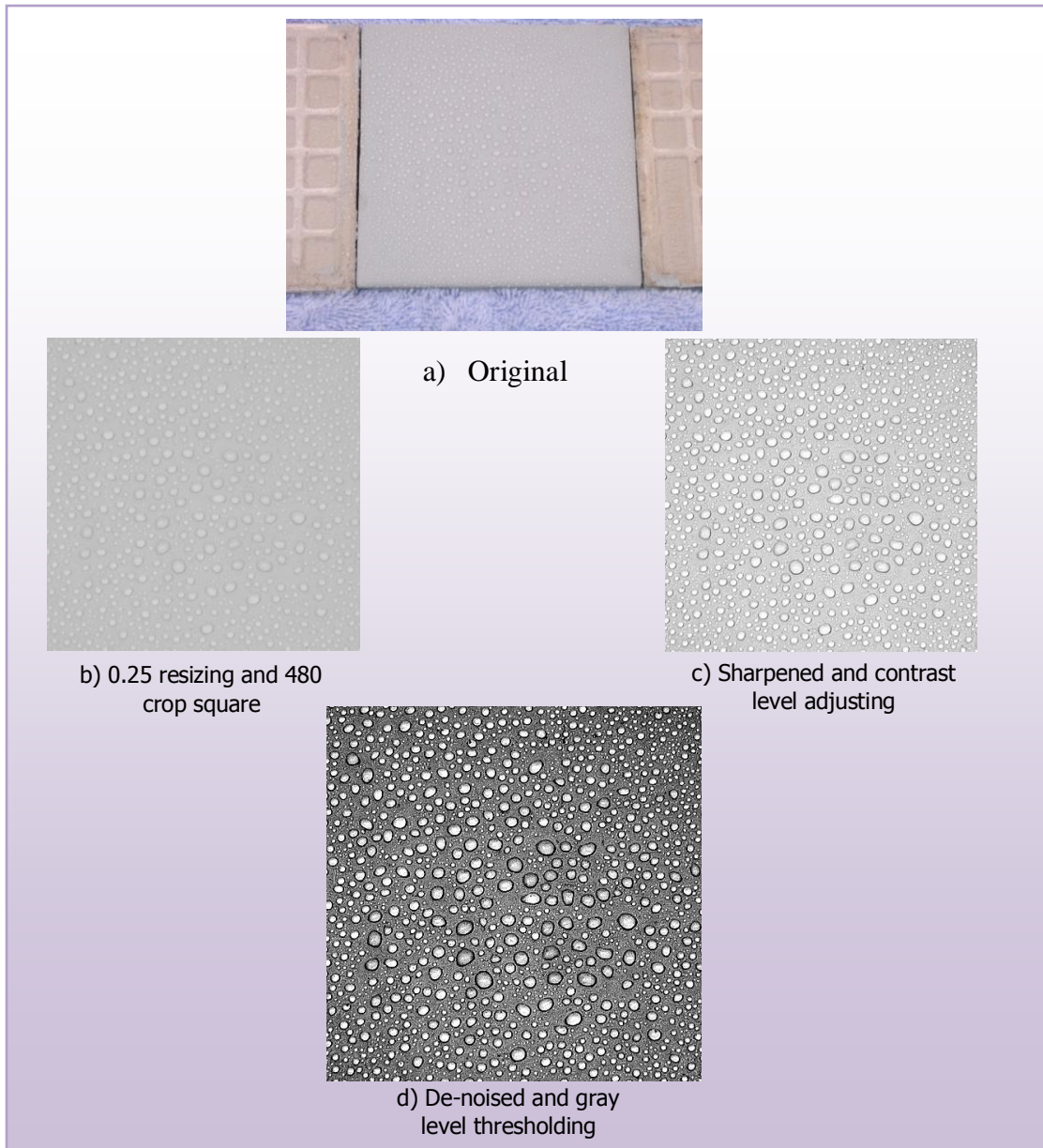


Figure 20. Image Preprocessing

2.3 Database Preparation and Description

A database of 358 gray level 481x481 sized images was prepared for the seven hydrophobicity classes as shown in Figure 21 using the preprocessing techniques described in Section 2.2. The prepared RTV coated tiles were sprayed with %ABV solutions for 1 minute according to the STRI guide to obtain the various HC images. Various %ABV solutions were prepared using a mixture of distilled water and surgical spirit that contained 68.6% ethyl alcohol and 3.7% methyl alcohol. The prepared number of samples for each hydrophobicity class is shown in Table 3.

Table 3. Database Summary

Class	HC01	HC02	HC03	HC04	HC05	HC06	HC07
No. of Images	44	49	42	41	67	63	52
% ABV	0%	10% & 20%	30%,40% & 50%	60% & 70%	80%	90%	100%

The tiles were placed at a 15 degree slope and at a distance of 400 cm from the camera. A FUJIFILM FINEPIX-JV200 camera was used with the following specifications as per the manufacturer manual [30]:

- Effective pixels: 14 million (14 Mega pixels)
- Lens: Fujinon 3x optical zoom lens F 3.1 (wide angle) – F 5.6 (telephoto) with focal length of $f = 6.5 \text{ mm} - 19.5 \text{ mm}$ (35-mm format equivalent: 36 mm – 108 mm)
- Digital zoom: approx. 6.7 x (up to 20.1 x when combined with optical zoom)
- File format: exif 2.3 JPEG (compressed)
- Aperture: F3.1/F8.0 (wide angle), F5.6/F14.4 (telephoto); uses Neutral Density (ND) filter
- Automatic white balance, automatic scene detection, tracking auto focus, digital image stabilizing, and auto flash mode.
- All the images were downsized by a factor of 4 and their intensity levels were equalized. A series of preprocessing steps including sharpening, contrast adjusting, and de-noising was applied to all the acquired images as per Section 2.2, in order to remove the redundancies and to enhance the distinguishing patterns in the images.

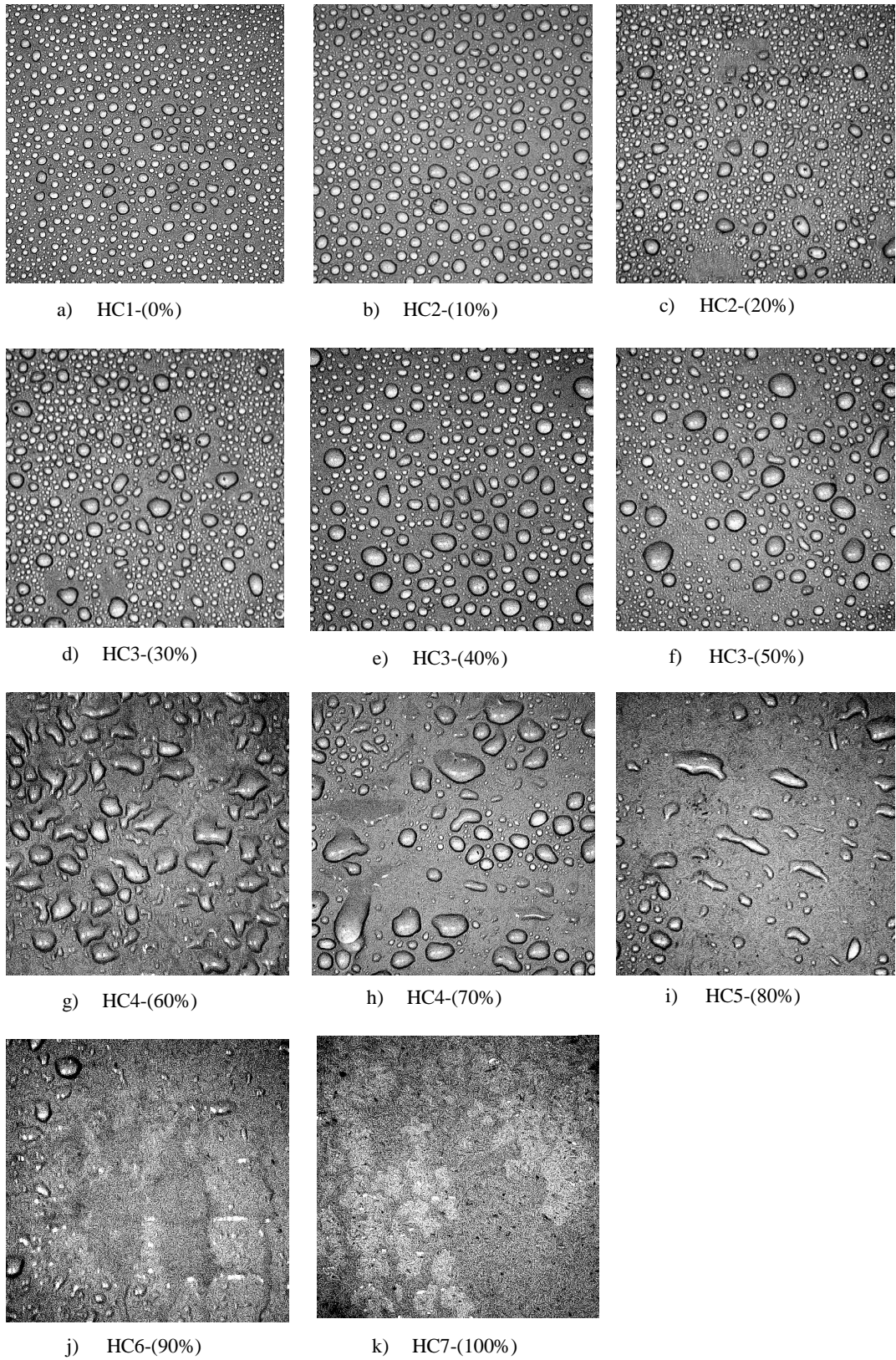


Figure 21. Samples of the Obtained Grayscale Database of the 7 HCs

CHAPTER 3: RESEARCH METHODOLOGY

This chapter describes the materials and methods used to develop the proposed system as demonstrated in Figure 22. It will also introduce a brief background about the techniques used and the theory behind them including digital image processing (DIP) and pattern recognition (PR) techniques.

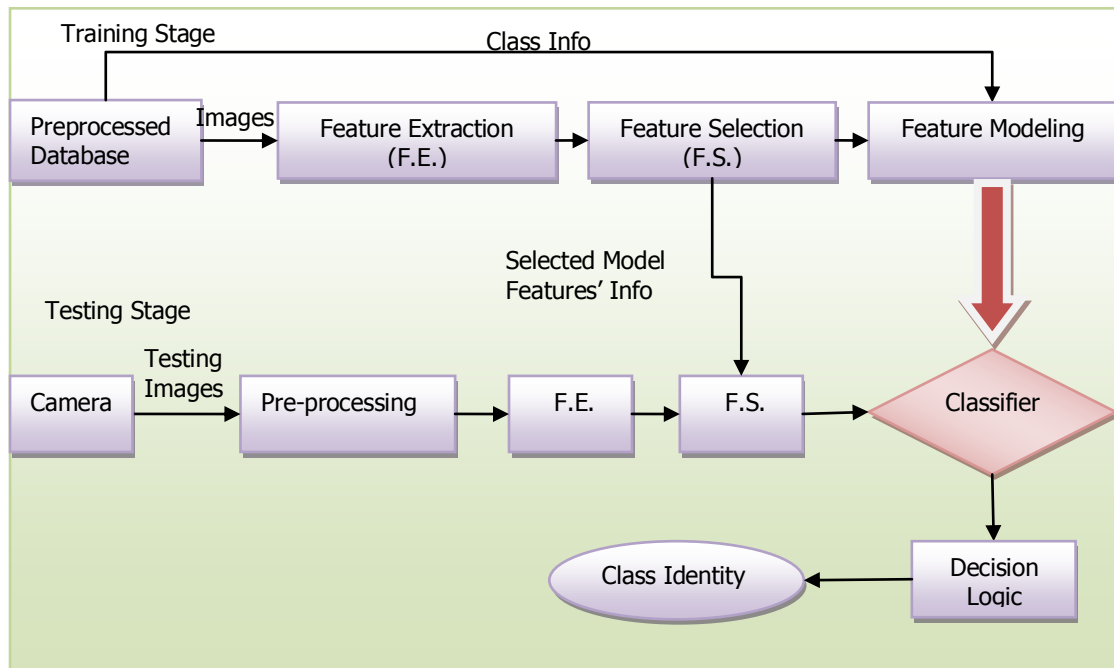


Figure 22. Proposed PR System

3.1 Feature Extraction

The data to be analyzed in this system is comprised of the images of the water droplets over the surface of the insulators of various hydrophobicity classes (HCs). To deal with this kind of input, the MATLAB DIP toolbox provides several functions that can help in preprocessing and extracting features from the images. More specifically, the image processing toolbox functions used for preprocessing include size reduction, color transformation, image enhancement and filtering techniques as discussed in the previous chapter. In this chapter, a variety of functions for image analysis and feature extraction were used including image moments and statistical parameters, image projections, Radon transform, contourlet transform, discrete cosine

transform, wavelet transform, gray level co-occurrence matrix (GLCM), and textural analysis.

3.1.1 Discrete Cosine Transform (DCT)

This transform represents the image as a sum of sinusoids of varying magnitudes and frequencies. It is very useful in image processing since most of the visually significant information about the image is concentrated in just a few coefficients of the DCT. The DCT function is given by Equation 3 [27], [29]:

$$D_{pq} = \alpha_p \cdot \alpha_q \sum_{m=0}^{M-1} \sum_{n=0}^{N-1} f(m, n) \cos\left(\frac{\pi(2m+1)p}{2M}\right) \cos\left(\frac{\pi(2n+1)q}{2N}\right) \quad (3)$$

where D_{pq} are the DCT coefficients, and α_p, α_q are given as in Equations 4 and 5 respectively:

$$\alpha_p = \begin{cases} \frac{1}{\sqrt{M}}, & p = 0 \\ \sqrt{\frac{2}{M}}, & 1 \leq p \leq M - 1 \end{cases} \quad (4)$$

$$\alpha_q = \begin{cases} \frac{1}{\sqrt{N}}, & q = 0 \\ \sqrt{\frac{2}{N}}, & 1 \leq q \leq N - 1 \end{cases} \quad (5)$$

The most significant components of the image are concentrated in the top left corner of the DCT images as shown in Figure 23. Using DCT on the obtained images allows us to represent the images in just 40 coefficients, instead of 231361 coefficients if the full image (with its size of 481x481) were to be used. The magnitude and phase angle of the DCT preserves the distinguishing features between the classes. The best way to extract the features from the DCT images is by applying the zigzag transform. The zigzag transform, also known as the zonal coding, implies that only the coefficients with the maximal variances are kept according to the zonal mask. The zigzag transform will rearrange the squared DCT image into a one-dimensional string. Figure 24 demonstrates the zigzag scanning scheme [29].

The one-dimensional string resulting from a zigzag transform consists of a DC coefficient as the first component and the rest represents the AC elements of the image. Figure 25 demonstrates a plot of the zigzag rearrangement of a class 5 DCT image.

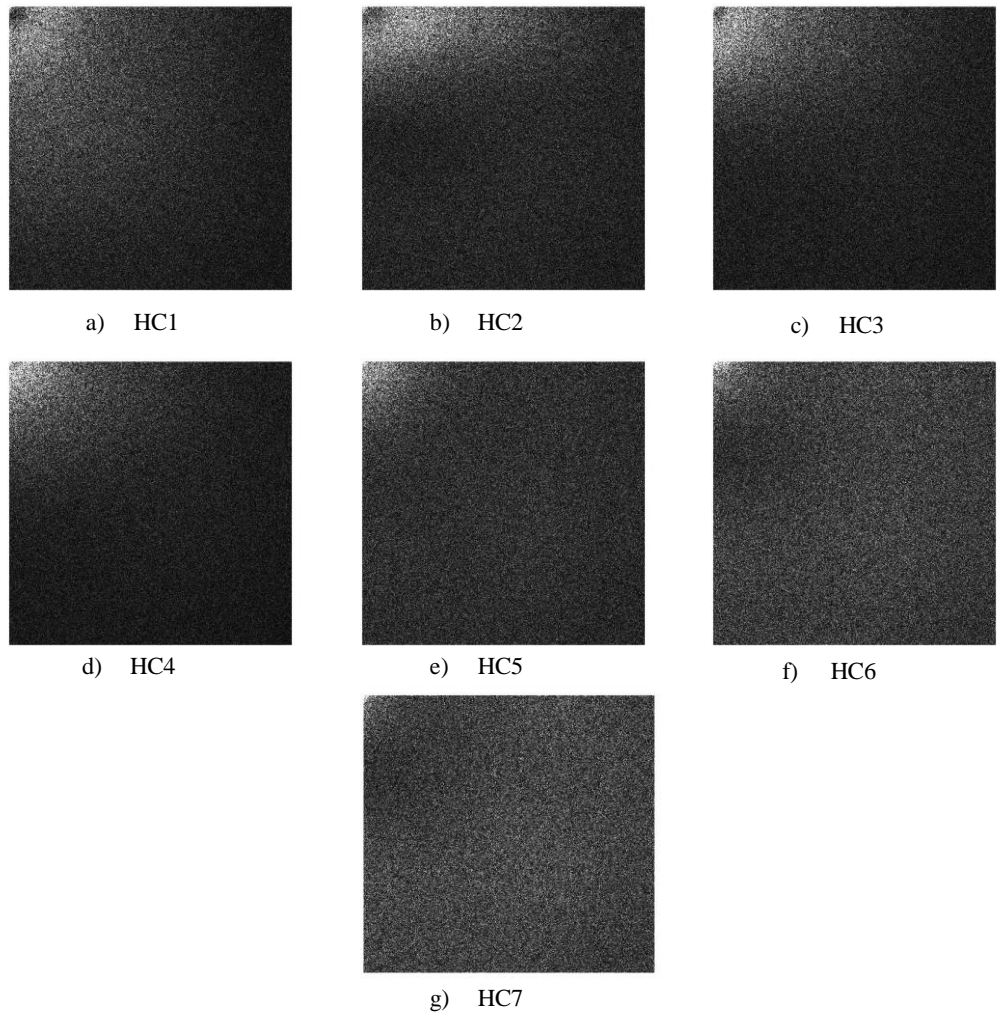


Figure 23. The Magnitude of the HC Images DCT

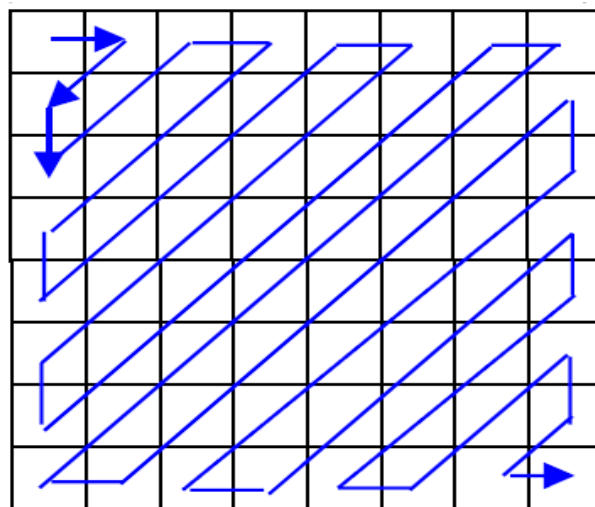


Figure 24. Zigzag Scanning Scheme [29]

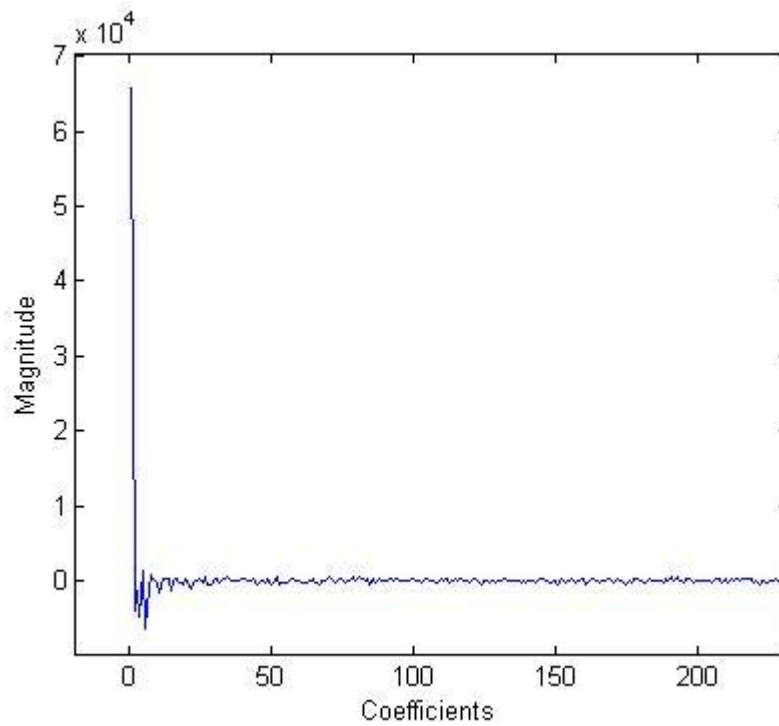


Figure 25. Zigzag Components of Class 5 DCT Image

The zigzag transform shown in Figure 25 has rearranged the DCT components with the most significant elements concentrated in the first 20-30 elements in this case. This allows us to drop the rest of the components as they don't add significant value to the desired feature vector (FV).

3.1.2 Projections and Radon Transform

A projection of a two-dimensional function $f(x, y)$ is a set of line integrals. The Radon function computes the line integrals from multiple sources along parallel paths, or beams, in a certain direction (any angle can be specified) according to Equations 6 and 7 as depicted in Figure 26. If the projection path is radiated by a single source, it is called a fan beam projection [27], [29].

$$R_{\theta}(x') = \int_{-\infty}^{\infty} f(x' \cos \theta - y' \sin \theta, x' \sin \theta + y' \cos \theta) dy' \quad (6)$$

where

$$\begin{bmatrix} x' \\ y' \end{bmatrix} = \begin{bmatrix} \cos \theta & \sin \theta \\ -\sin \theta & \cos \theta \end{bmatrix} \begin{bmatrix} x \\ y \end{bmatrix} \quad (7)$$

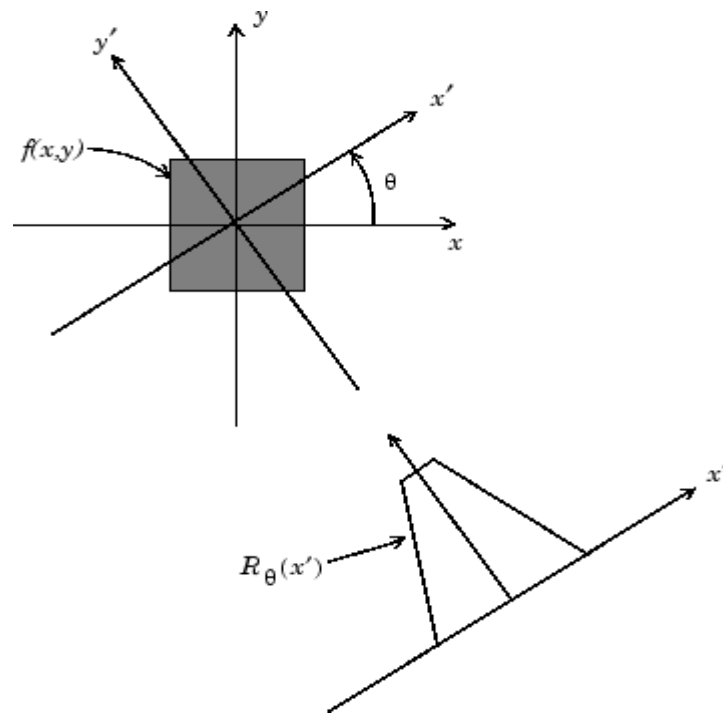


Figure 26. Radon Transform Geometry [29]

The Radon transform projects the data of the images into a one-dimensional string radiated from one source depending on the angle of projection [29]. The angle of projection in this research has no significance since the water droplets are distributed randomly over the whole surface of the insulator. Whether it's an X or Y axis projection, the resulted beam will preserve significant information about the area and the shape of the water droplets which are of a distinguishing nature between different HC classes as demonstrated in Figures 27 and 28, respectively.

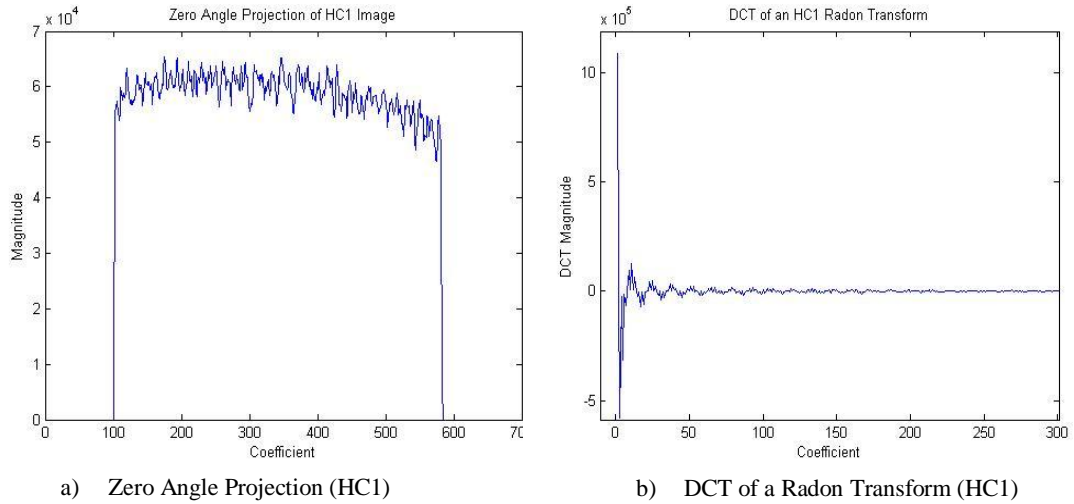


Figure 27. Zero Angle Radon Transform of an HC1 Image

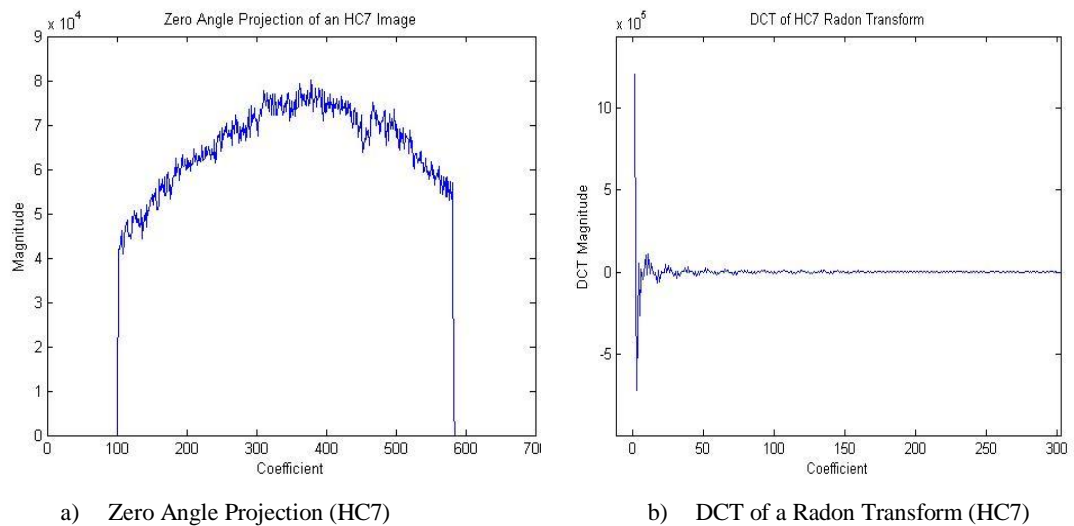


Figure 28. Zero Angle Radon Transform of an HC7 Image

Since the Radon transform reflects the shape, area, and distribution of the droplets, one can notice the variation of the Radon coefficients' magnitudes and frequencies. As the insulator class moves up from class one to seven, the magnitude of the spikes, which relates to the general uniformity in the height of the droplets projected, declines. This is directly related to the nature of the droplets in different classes since they move down from small droplets with a 90^0 contact angle to a completely wetted area with a uniform surface. The variation of the size of the droplets can also be

extracted between the classes as the base frequency seems to get higher with the classes, indicating the largest droplet/wetted area between the classes.

3.1.3 Wavelets Transform

Similar to the one-dimensional wavelets, the discrete wavelets transform (DWT) can be generalized to higher dimensional signals. In image processing, DWT has a great influence since it allows us to analyze images in different scales. Unlike the Fourier transform, DWT decomposes the acquired images into different levels based on their frequencies while preserving their location in time. The decomposed components are correlated to the effective frequency of the mother wavelet. The images are passed through a series of filter banks consisting of several low-pass and high-pass filters depending on the level of decomposition [26] as shown in Figure 29.

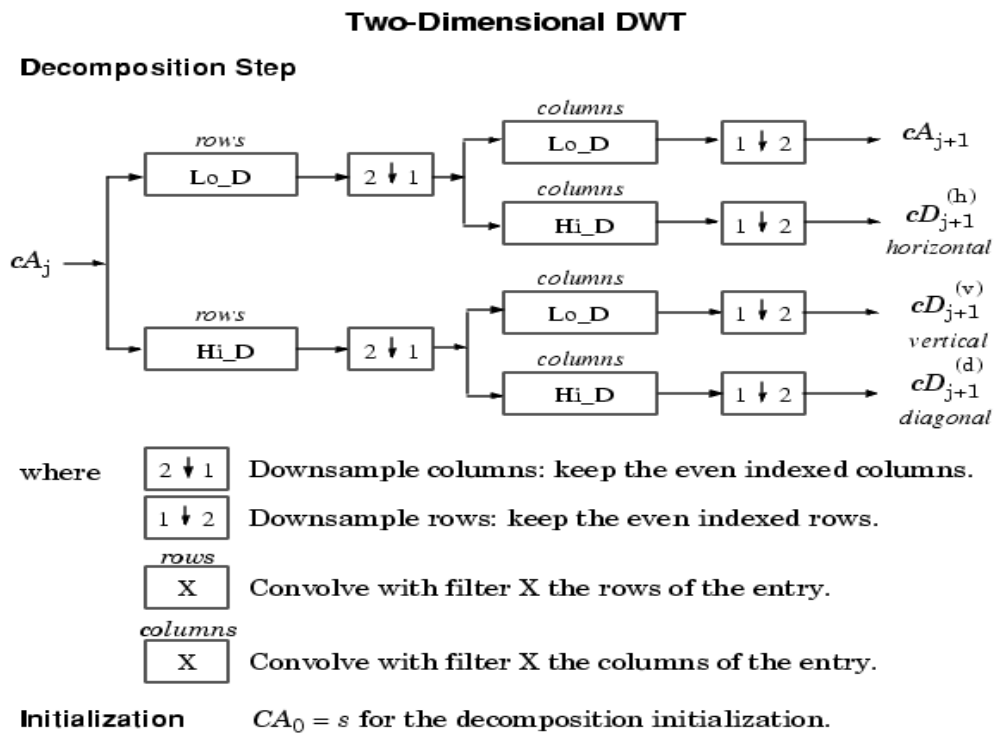


Figure 29. Two Dimensional DWT Decomposition Process [26]

The resulting decomposition of the high-pass filter are the “details” which characterize the high-frequency content of the image in a certain band. The low-pass filter output represents the “approximations” which are the low-frequency content of that band. The decomposition of an image can be broken down into two stages as

demonstrated earlier in Figure 29. The first stage involves the decomposition along the x-axis while the second stage is to convolve the output with the filter banks along the y-axis which will result in a four band output: low-low band (LL), low-high band (LH), high-low band (HL), and high-high band (HH) [26]. As shown in Figure 30, the power is further concentrated in the LL band which contains the approximation coefficients. On the other hand, the HL, LH, and HH bands contain the variation along the x-axis (horizontal coefficients), the y-axis variations (vertical coefficients), and the diagonal coefficients, respectively. The “approximation” (LL band) is shown in the top-left, while the “details” bands (HL, LH, and HH) are in the top-right, bottom-left, and bottom-right, respectively. Similarly, the process will continue for higher decomposition levels on the approximation band as shown in Figure 31.

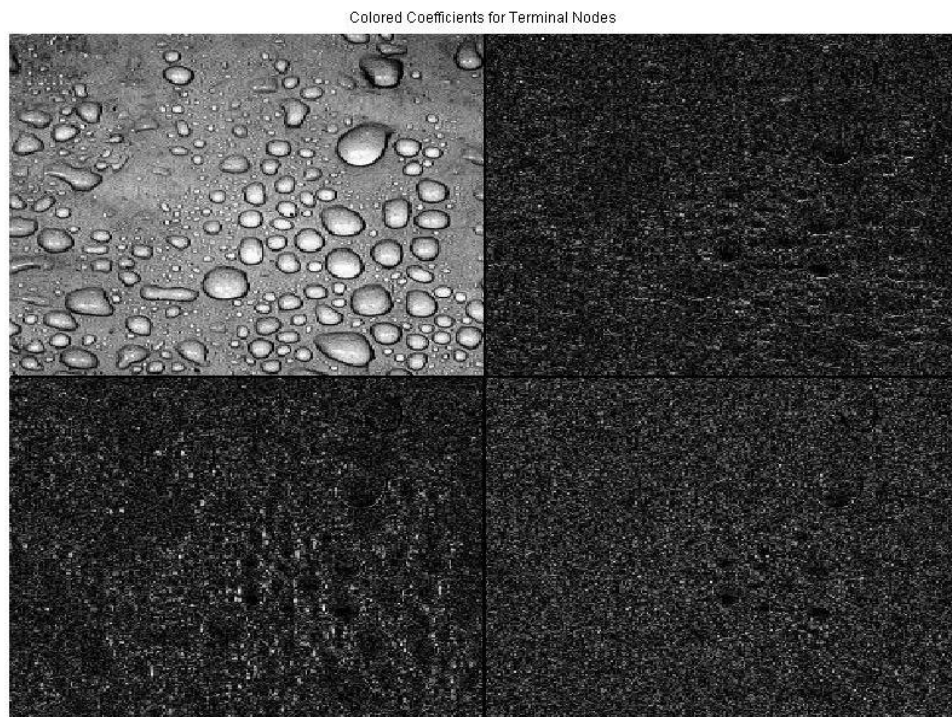


Figure 30. 1-Level Decomposition Using Haar Wavelet

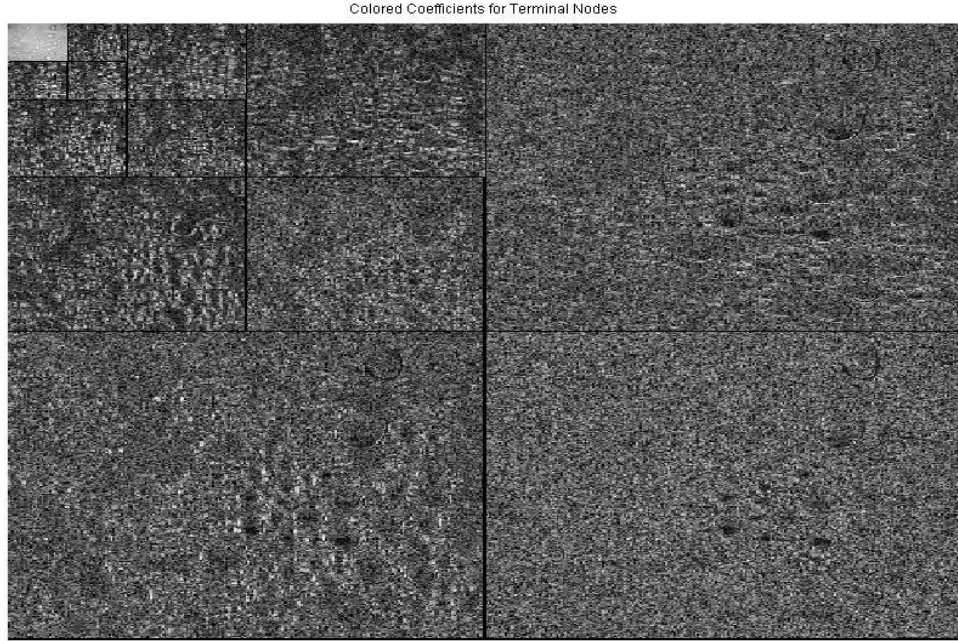


Figure 31. 4-Level Decomposition Using Haar Wavelet

Several features can be extracted from each band to construct the FV such as the entropy, mean, variance, and energy.

- Entropy:

DWT entropy is a statistical evaluation of the energy scattering between various spectral bands. Principally it measures the focus of coefficients in a particular band. The entropy of a certain band is given by Equation 8 [29]:

$$E = -\sum x_i^2 * \log(x_i^2), 1 \leq i \leq N \quad (8)$$

where E is the entropy of the band, x is the string of the coefficients, and N is the number of coefficients.

- Mean:

The wavelet mean value is a statistical measure of the average of the coefficient in each band and is obtained from Equation 9 [29]:

$$Mean : \mu = \frac{\sum x_i}{N}, 1 \leq i \leq N \quad (9)$$

- Variance:

Variance is a statistical measure of how the data is spread out. In other words, it's a measure of the stretch between the coefficients in each band and is obtained by Equation 10:

$$\text{Variance: } \sigma^2 = \frac{\sum(x_i - \mu)^2}{N} \quad (10)$$

- Wavelet Energy:

Wavelet energy refers to the energy percentage of the decomposition bands of the wavelets. The percentage energy of each of the “approximation” and “details” band is calculated as per Equation 11:

$$W_energy = 100 * \frac{\sum x_i^2}{E_t} \quad (11)$$

where E_t is the total energy of the “approximation” and the “details” bands.

3.1.4 Contourlet Transform

Since the images in this research have discontinuity points such as edges and demonstrate intrinsic geometrical structures that contribute to the distinguishing features between the HC classes, the work of the wavelet while isolating these singularities might fail to capture the smoothness among the image contours. The contourlet transform overcomes the limitation of DWT by applying various basis elements consisting of several shapes and aspect ratios to capture the smooth contours and lines in the images. Moreover, these bases are applied at an array of angles and directions to easily capture the directionality factor in the images. The concept behind the contourlet transform is to apply an edge detection algorithm using a wavelet-like transform and then utilizing a local directional transform to detect the contour segments [26]. Unlike DWT, the contourlet transform uses a double filter bank structure as shown in Figure 32. The first stage utilizes a laplacian pyramid filter to detect singularities, which results in an approximation band and a difference band. The approximation band is further decomposed based on the level of decomposition. The obtained decompositions are then passed through a directional filter bank in order to link the discontinuity points into smooth lines similar to the Hough transform [26].

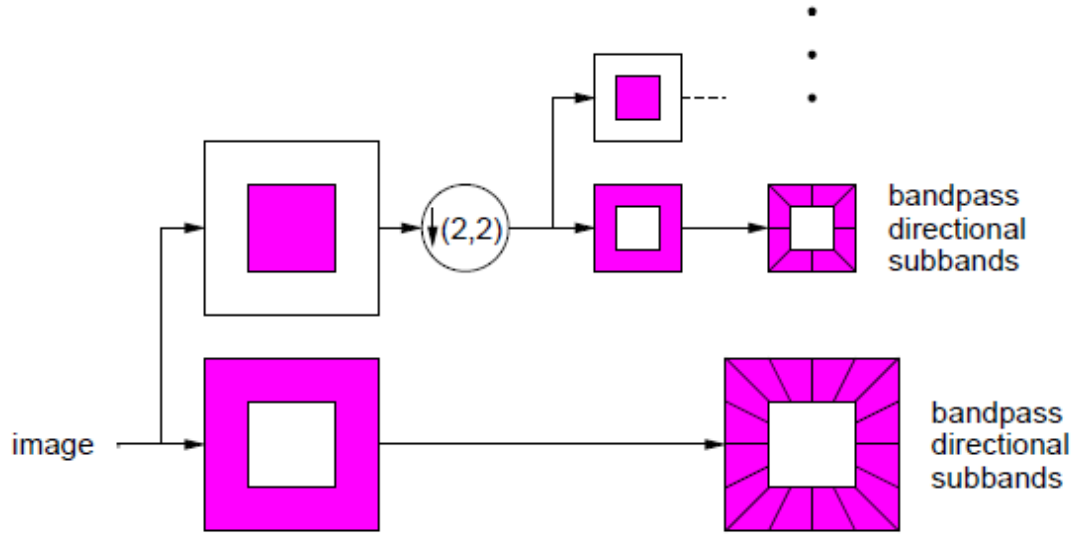


Figure 32. Contourlet Transform's Double Filter Bank Structure [26]

The resulting image expansion is a product of the laplacian pyramid filter levels and the directional filter levels. Several features can be extracted from the resulting decompositions including statistical features such as entropy, energy, mean, and variance, or textural features using the gray level co-occurrence matrix (GLCM) on each of the bands.

3.1.5 Gray Level Co-Occurrence Matrix (GLCM)

The GLCM function is a method of analyzing the textural features of an image. By considering the spatial correlation between the images' pixels, the GLCM returns what could be considered second-order statistical features. Based on the offset specified (distance and angle), the GLCM calculates how often a certain intensity level “i” co-occurs with an intensity level of a pixel with a “j” value. If GLCM is considered a statistical probability measurement of the gray level variation between two intensity levels (i , j), then Equation 12 best describes the GLCM function [31]:

$$P(i, j | \Delta x, \Delta y) = \frac{1}{W} \sum_{n=1}^{N-\Delta y} \sum_{m=1}^{M-\Delta x} \begin{cases} 1, & \text{if } f(m, n) = i \text{ and } f(m + \Delta x, n + \Delta y) = j \\ 0, & \text{elsewhere} \end{cases} \quad (12)$$

and

$$W = \frac{1}{(M-\Delta x)(N-\Delta y)}, \quad (13)$$

where $f(m, n)$ is the intensity level at pixel (m, n) , and $(\Delta x, \Delta y)$ is the offset. Table 4 provides examples of the offset values.

Table 4. Offset Values for the GLCM

$(\Delta x, \Delta y)$	Offset
$(a, 0)$	0^0 angle with distance a
$(0, b)$	90^0 angle with distance b
(a, b)	$\tan^{-1}(\frac{b}{a})$ angle, i.e. 45^0 if $a=b$.

The GLCM matrix can be considered a feature vector itself if the right gray level is used. Other statistical features can be extracted also from the GLCM matrix as in Table 5. In addition to extracting statistical and textural features by applying the GLCM directly to images, GLCM can also be used to extract features from other image processing tools such as the wavelet and the contourlet transforms. In general, other useful transforms and operations can also be used to detect lines, peaks, angles, and edges, or in general analysis of the images. Examples of those transforms are Hough transform, morphological operations (dilation and erosion), skeletonization, distance transforms, and polynomial fitting. All of these transforms and operations and several others can be used in image enhancement, analysis, representation, and feature extraction in order to form the feature vector (FV) in the PR system.

Table 5. Description of the GLCM-Based Features

Statistic	Description
Contrast	A measure of the local variations in the GLCM matrix
Correlation	A measure of the joint probability occurrence of selected pixel pairs.
Energy	The sum of squared coefficients in the GLCM, which is referred to in GLCM analysis as the image uniformity or the angular second moment.
Homogeneity	A measure of the proximity in the distribution of the GLCM elements to the GLCM diagonal.

3.2 Feature Selection

In this research, the stepwise regression is used as a feature selection method. The stepwise regression helps in selecting the most contributing features to our model and hence helps reduce the size of the feature vector. Depending on the statistical significance of the features, the stepwise regression will discard the redundant or unrelated features. The stepwise regression uses the F-statistic parameter in its selection process, which is a measure of the contribution of the selected term to the dependent variables. It is calculated as per Equation 14 [32]:

$$F_j = \frac{SSR(\beta_j|\beta_0, \beta_1, \dots, \beta_{j-1}, \beta_{j+1}, \dots, \beta_k)}{MS_E} \quad (14)$$

where;

β_j is the regression coefficient based on the current added feature x_j

$\beta_0, \beta_1, \dots, \beta_{j-1}, \beta_{j+1}, \dots, \beta_k$: are the regression coefficients of the current model features

MS_E is the mean square error of the model features

$SSR(\beta_j|\beta_0, \beta_1, \dots, \beta_{j-1}, \beta_{j+1}, \dots, \beta_k)$ is the regression sum of squares due to a specific regression coefficient (β_j) given the current regression coefficient in the model.

The process of adding and removing coefficients from the feature vector is determined based on the p-value of that coefficient which signifies the null-hypothesis probability with acceptance tolerance of α for adding a feature, and a rejection tolerance of β for removing one. The initial model usually starts with the feature of the least p-value. The selection continues by adding features to the model and calculating the p-value in each step. Next the algorithm looks at whether the feature adds significance to the model or not as per the simplified flow chart in Figure 33 [33].

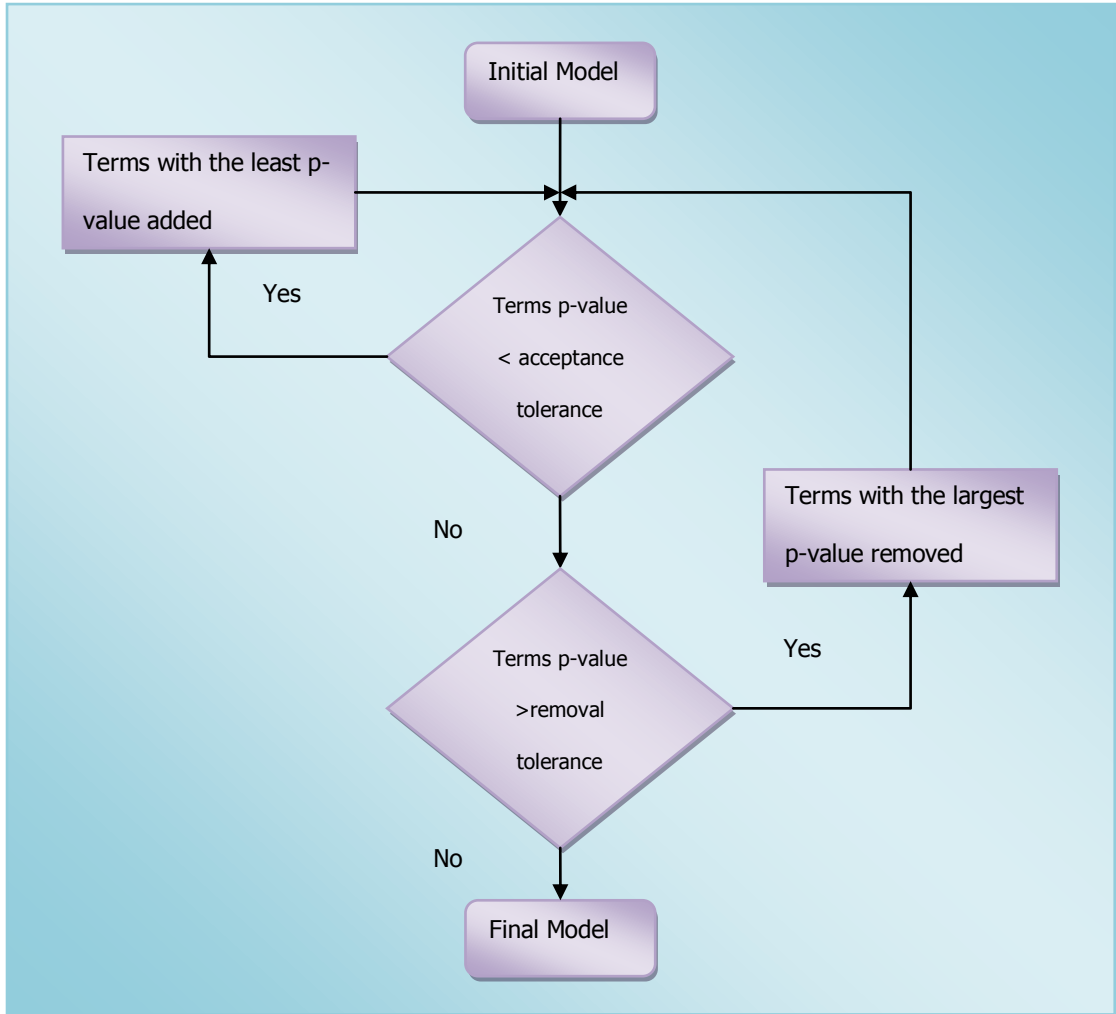


Figure 33. Stepwise Regression Process

The final model varies based on the terms selected in the initial model and the values of the acceptance and removal tolerances. To find the best representative model, the R^2 -statistic and F-statistic are calculated for each suggested model. The R^2 -statistic indicates the ratio of deviation for the predicted variable from the current features in the selected model and is calculated as per Equation 15 [33].

$$R^2 = \frac{SSR}{SST} = 1 - \frac{SSE}{SST} \quad (15)$$

where

$SSR = \sum_{n=1}^N (\hat{Y}_t - \bar{Y})^2$: The sum of the squares regression

$SST = \sum_{n=1}^N (Y_t - \bar{Y})^2$: The sum of squares total

$SSE = \sum_{n=1}^N (Y_t - \hat{Y}_t)^2$: The sum of squares error

Y_t : The added actual feature

\bar{Y} : The mean value of the feature from the training data

\hat{Y}_t : The suggested term based on the selected fitted model

N: the number of the training images

The model with an R^2 -statistic equal to 1 indicates the best regression model while a zero R^2 -statistic value corresponds to the worst-fitting model.

3.3 Pattern Recognition System

Pattern recognition (PR) is a means of assigning objects or events to one of several pre-specified categories (classes) [34]. In this proposed system, the objects are the images of the insulators' wetted surfaces, and the categories are the hydrophobicity classes. A typical PR system consists of the following stages as demonstrated in Figure 34.

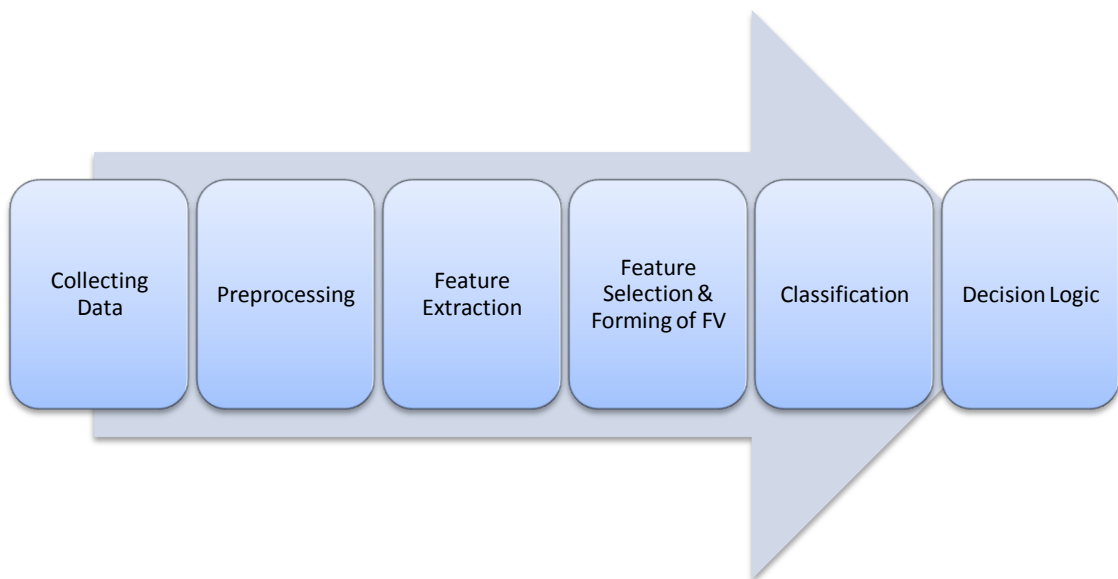


Figure 34. PR Structure

The first four steps were covered in the previous sections. In the classification stage, extracted features are mapped into the seven different classes. The choice of classifier depends on the features extracted in the previous stage. Prior to training and evaluating of the classifier, it is quite common for feature selection to be required to reduce the dimensionality of the feature space. A post-processing stage may also be

required to utilize the context, input depending information, improve the system performance, and reach the correct decision. Similar to what was done in Section 3.1 and for the benefit of the reader, the following PR background is given. In general, a classifier can be viewed as a network that computes m discriminant functions and selects a category corresponding to the largest discriminant [34] as demonstrated in Figure 35.

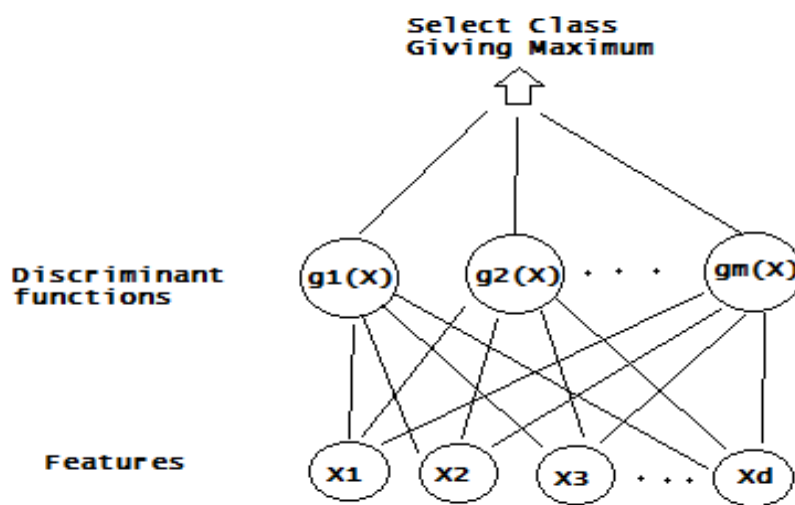


Figure 35. General Representation of a Classifier [34]

PR theory provides several classifier designs to choose from depending on the nature and distribution of the features. These classifiers can be categorized depending on the spread of the data in the feature space into linear and nonlinear classifiers.

3.3.1 Linear Classifiers

The discriminant function could be linear if the features are linearly separable. A linear discriminant function is given by Equation 16 [34].

$$g_i(x) = w^t x + w_0 \quad (16)$$

where w^t represents the weights of the separation line and w_0 is the offset of the line. Discriminant functions can be more general than a separation line. If the data are

normally distributed, several classifiers can be chosen such as the maximum likelihood (ML) classifier (shown in Equation 17) or the Bayes classifier which can be of Euclidean or Mahalanobis distance-based. Equation 18 shows a general form of a Bayes classifier [35].

$$P(X|C) = \frac{1}{(2\pi)^{\frac{d}{2}} |\Sigma|^{-\frac{1}{2}}} \exp \left[-\frac{1}{2} (X - \mu)^t \Sigma^{-1} (X - \mu) \right] \quad (17)$$

$$g_i(x) = x^t w x + w^t x + w_0 \quad (18)$$

The parameters of the classifier such as the mean (μ) and covariance matrix (Σ) can be estimated from the training data using parametric techniques such as Bayesian estimation or ML estimation (MLE). Equations 19 and 20 demonstrate the MLE of the mean vector and covariance matrix for a given feature vector [35].

$$\mu = \frac{1}{n} \sum_1^n X_i \quad (19)$$

$$\Sigma = \frac{1}{n} \sum_1^n (X_i - \mu)(X_i - \mu)^t \quad (20)$$

3.3.2 Nonlinear Classifiers

3.3.2.1 Polynomial Classifier

Nonlinear classifiers are used to handle linearly non-separable data. One of the important algorithms for doing so is the polynomial classifier. The main concept of polynomial classifiers is to divide the feature space into a set of hyper-planes that separate different classes by the largest gap or distance to the nearest training data points of any class [32]. The polynomial classification depends on expanding the feature vector space into higher-order space to find a separating plane or hyper plane on that space. The difference between the polynomial and linear classifiers is the kernel function that separates the classes from each other. This difference is used to map the training data into the kernel choices. Most often when the data is not linearly separable in one space, it might be so in higher spaces. The polynomial classifier can be of any order which maps the data into a different space (usually higher space) so it can be linearly separable in that space [36-37]. Figure 36 demonstrates the expanding process of the feature vector for a second-order polynomial classifier. Unfortunately this comes at the expense of increasing the computational cost greatly and for a large data bank it might take several minutes to compute the weights of the classifier. Also, there is always the possibility of falling into the curse of dimensionality [37].

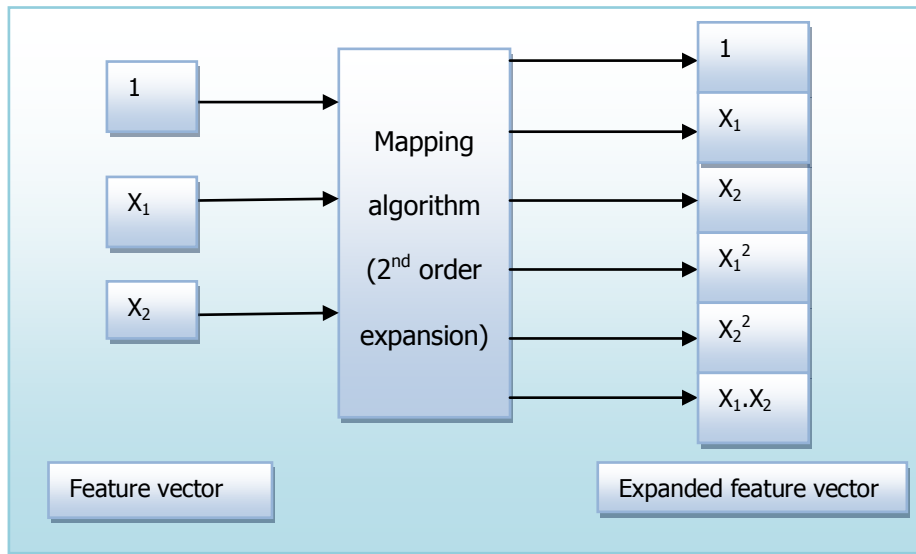


Figure 36. Second Order Polynomial Expansion of a 2-Dimensional Feature Space

Therefore, dimensionality reduction techniques become necessary in this case. An example of such a technique is the stepwise regression discussed in Section 3.2.

3.3.2.2 K-Nearest Neighbor

The K-Nearest Neighbor (KNN) is one of the simplest, most effective classifiers in machine learning algorithms. The concept of the KNN is to compare the testing FV to the training FVs of different classes searching for the closest FV in the training feature space. One of the most desirable features in the KNN algorithm is its instant-based learning which doesn't require pre-training to determine the classes of the feature spaces. Depending on the choice of K neighbors, the KNN algorithm classifies new objects by the majority votes found between their neighbors. For instance, if K is chosen to be 1, then the algorithm is simply finding the class of the closest sample to the test objects. Likewise, if K is chosen to be 3, then the classified class will be the one with the 2 or more votes [35]. The choice of K is very important in determining the best classification algorithm and reducing error rate. If K is chosen to be very small, then the noise within the data will have a great effect on the decision. On the other hand, a large K will reduce the effect of noise but will reduce the recognition rate near the boundaries. The distance algorithm commonly used in KNN is the Euclidian distance which measures the metric distance between the test

sample and the training samples. Other distance algorithms used include the hamming distance and the cluster center distance. The performance of the KNN could be improved by scaling the features based on their importance to eliminate the effect of irrelevant features using the mutual information algorithm or the evolutionary algorithms. Distance measuring could also be improved using a training algorithm such as the large margin nearest neighbor [35].

3.3.2.3 Artificial Neural Network

Another important type of classifiers is the artificial neural network (ANN). Similar to a biological neural network, ANN consists of interconnected neurons that collect signals from inputs and from each other, process them inside the neuron body, and fire up an output signal accordingly.

ANN can be simplified into a three-layered structure [34]:

1. Input Layer: This includes the features and the bias unit. The activation of the input layer could be of a linear type as a weighting scheme of the importance of the feature.
2. Hidden layer(s): The hidden layer could be made of a single layer of activation functions that collects the signals from the input layers or multiple hidden layers with proper activation functions. The activation function of the hidden layer is essentially nonlinear to allow for nonlinear decision regions. Activation functions can be categorized as [34]:

- Discontinuous activation functions (Equation 21 gives an example).

$$F(Net_k) = \begin{cases} 1, & Net_k \geq 0 \\ -1, & Net_k < 0 \end{cases} \quad (21)$$

- Continuous activation functions (Equation 22 gives an example of a sigmoid function).

$$F(Net) = \alpha \cdot \frac{e^{\beta \cdot Net} - e^{-\beta \cdot Net}}{e^{\beta \cdot Net} + e^{-\beta \cdot Net}} \quad (22)$$

where α and β are constants and are often set to 1.716, and 2/3, respectively. Continuous activation functions are differentiable and hence allow the use of the gradient descent learning.

3. Output layer: The job of this layer is to collect the final outputs of the last hidden layer and produce m outputs, 1 for each class.

Accordingly, the output of the ANN can be calculated based on Equation 23. Figure 37 demonstrates the structure of a Feed Forward (FF) ANN:

$$Z_k = F\left(\sum_{j=1}^{N_H} V_{kj} F\left(\sum_{i=1}^d W_{ji} X^i + W_{j0}\right) + V_{k0}\right) \quad (23)$$

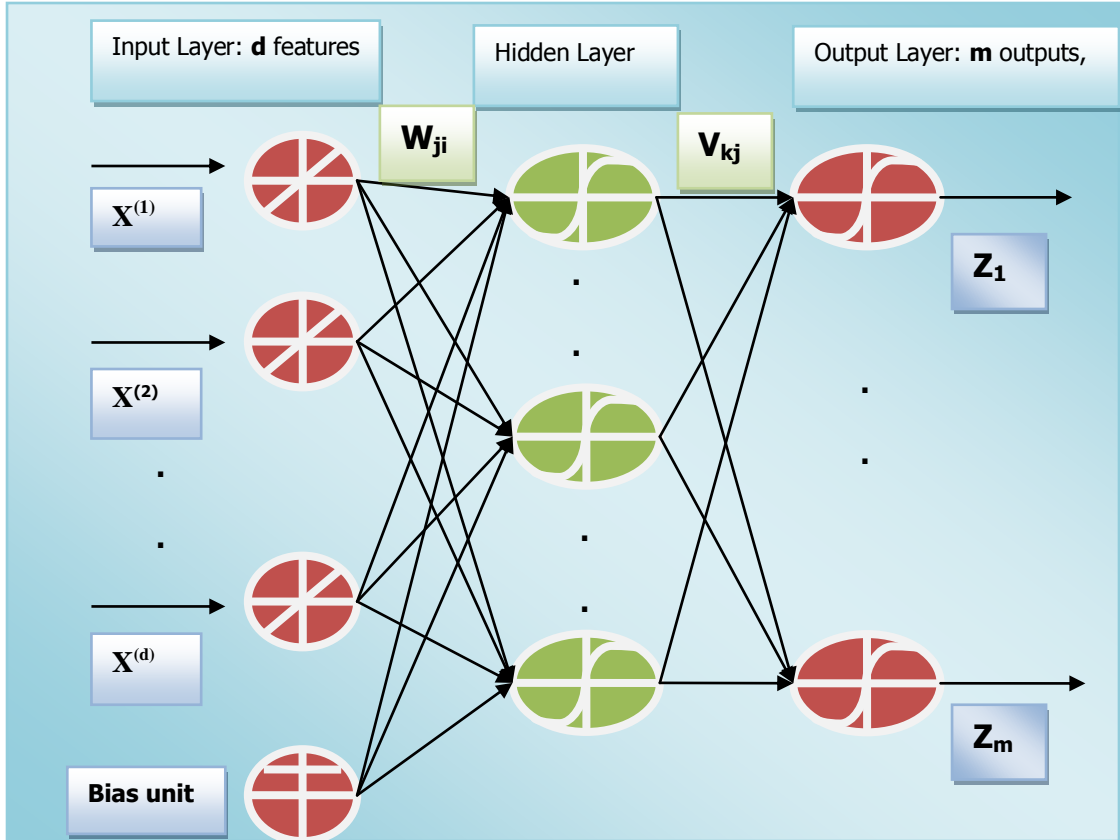


Figure 37. Structure of FF ANN

The output of the ANN can be calculated according to Equation 23, and the weights, W and V , can be initialized to any non-zero values. To update the values of the weights, the output (Z) should be compared to a target output (t). One of the most common techniques for updating the weights of the ANN is using the back propagation (BP) algorithm. Whether using a stochastic (sample by sample learning) or batch-based technique, a BP computes the total learning error according to Equation 24 [35].

$$J(W, V) = \frac{1}{2} \cdot \sum_{i=1}^n \sum_{c=1}^m (t_c^i - Z_c^i)^2 \quad (24)$$

The weights then will be updated using the gradient descent method as in Equations 25 and 26.

$$W^{t+1} = W^t - \eta \nabla_w J(W^t) \quad (25)$$

$$V^{t+1} = V^t - \eta \nabla_v J(V^t) \quad (26)$$

where

η = the learning rate, which determines the speed of the learning process.

The process will start again by FF operation with the updated weights, and the BP will continue updating the weights until convergence (output (Z) = target (t) with some tolerance $J < \epsilon$) or the preset number of iterations is reached [34]. In this research, η was optimized to 0.73 with a 0.1 tolerance and a maximum of 30 iterations.

CHAPTER 4: RESULTS AND DISCUSSION

This chapter will present the recognition rates achieved using different combinations of feature extraction and dimensionality reduction schemes, and classification methods. The discussion will also include an assessment of the effectiveness of combining (fusing) a collection of different sets of features including statistical, textural, and spectral features extracted using various techniques. Also, the impact of using dimensionality reduction techniques on the recognition rates and numerical stability will be investigated. Various models will be discussed throughout the chapter. The aim is to reach an optimum model and determine the most suitable ways of classifying silicone rubber insulator hydrophobicity classes (HC). The results presented in this chapter represent the outcomes of a round Robin technique to eliminate the bias effect. That is, the samples from each class were divided into 4 categories. Then, while maintaining a random selection of the categories in each round Robin run, two out of the four categories from each of the seven classes' samples were accordingly assigned to the training samples and the others to the testing samples, and so on.

4.1 Discrete Cosine Transform (DCT) Based Features

In this feature extraction scheme, the feature vector (FV) is extracted using the DCT algorithm on the HC image database discussed earlier. A zonal coding methodology, also known as a zigzag transform (ZT), is used to determine the optimal FV of a certain length to represent the image. Table 6 shows the recognition rates using absolute values of DCT coefficients of various lengths as feature vectors (FV) with different classification techniques. The linear classifier shows a steady improvement in the recognition rate from 59% to 76% as the number of DCT features increases from 10 to 40 features. Further increases in the feature vector size result in a decline in the recognition rate. On the other hand, the polynomial classifier achieved a 72.51% recognition rate when the number of the features was only 10, as opposed to a 59.1% rate with the linear classifier. Further increases in the feature vector size led to a drop in the recognition rate as a result of numerical instability which can be alleviated by the use of dimensionality reduction techniques. While the KNN classifier shows a slightly lower recognition rate compared to the linear classifier, the

ANN shows the best recognition rate among all classifiers by achieving 80.12% when 15 features and 30 neurons were used.

Table 6. Recognition Rates of the DCT Absolute Value FV

Classifier \ FV-length	10	15	20	30	40	50	60
	Recognition Rate						
linear	59.1%	68.4%	70.76%	73.10%	76.02%	74.85%	70.18%
Polynomial 2 nd	72.51%	67.25%	39.18%	38.59%	46.2%	45.61%	49.71%
KNN:1	67.25%	71.34%	73.10%	68.42%	68.42%	69.59%	67.25%
KNN:3	66.08%	65.49%	63.70%	67.83%	66.67%	69.59%	64.9%
KNN:5	61.99%	64.90%	66.08%	67.83%	65.5%	65.5%	61.4%
NN network (5 neurons)	65.49%	68.42%	76.02%	69.59%	67.83%	59.64%	59.64%
NN network (10 neurons)	73.10%	76.60%	70.17%	67.83%	73.68%	61.40%	61.40%
NN network (15 neurons)	70.17%	74.85%	74.26%	72.51%	64.91%	61.40%	67.83%
NN network (20 neurons)	76.02%	79.53%	74.85%	78.94%	75.43%	71.34%	75.43%
NN network (25 neurons)	74.27%	77.19%	76.02%	73.10%	74.85%	73.10%	74.85%
NN network (30 neurons)	73.68%	80.12%	78.36%	76.02%	78.94%	74.85%	73.10%
NN network (40 neurons)	74.85%	74.27%	76.02%	78.36%	77.19%	76.60%	77.19%

Although the magnitude of the DCT is considered an important feature in the classification process, incorporating the sign of the DCT coefficients further enhanced the recognition rate as demonstrated in Table 7. The linear classifier rate increased to around 80% while the highest rate of 86.55% was achieved using the KNN-1 classifier. A recognition rate of 83.63% was achieved using the ANN with 25 neurons and a feature vector of 30 elements. Again, the polynomial classifier recognition rate dropped significantly when the size of the feature vector increased beyond 10, most likely due to numerical instability. So it is important to use the

dimensionality reduction technique to test the effectiveness of the polynomial classifier and to reduce the computational cost of all other classifiers.

Table 7. DCT Magnitude and Phase FV Recognition Rates

Classifier \ FV-Length	10	15	20	30	40	50	60
	Recognition Rate						
Linear	63.2%	71.3%	76.61%	76.02%	79.53%	79.53%	77.78%
Polynomial 2 nd	72.51%	58.4795	36.25%	Rank deficient matrix			
KNN:1	82.46%	84.79%	86.55%	86.55%	84.80%	85.96%	84.79%
KNN:3	76.60%	79.53%	81.87%	81.87%	81.87%	81.29%	81.87%
KNN:5	74.26%	76.02%	78.95%	78.95%	78.95%	78.95%	80.117
NN network (5 neurons)	72.51%	75.44%	76.61%	76.61%	70.76%	69.59%	76.61%
NN network (10 neurons)	76.02%	78.95%	77.19%	71.35%	78.95%	81.87%	81.29%
NN network (15 neurons)	76.02%	81.87%	81.29%	73.68%	73.10%	73.68%	81.87%
NN network (20 neurons)	77.19%	84.21%	81.29%	81.29%	79.53%	74.27%	81.29%
NN network (25 neurons)	74.27%	82.46%	81.29%	83.63%	73.68%	74.85%	83.63%
NN network (30 neurons)	81.29%	81.87%	80.12%	82.46%	79.53%	77.19%	82.46%
NN network (40 neurons)	78.36%	82.46%	81.87%	82.46%	81.87%	81.29%	82.46%

Table 8 demonstrates the effect of stepwise regression on the result of the classification. After using stepwise regression, it appears that most significant components of the FV concentrate in the first 40 features of the ZT since the output features from the stepwise regression only increase by 1 element when the size of the FV increases from 40 to 70. Also, the polynomial classifier performance is enhanced considerably once the issue of rank deficiency was resolved. The recognition rates achieved by the KNN and ANN classifiers were better than that of the polynomial classifier which indicates that numerical instability (i.e., a high condition number) was still not completely resolved. This will be further discussed in Section 4.7.

Table 8. DCT Features' Recognition Rates with Stepwise Regression

Classifier \ FV- Length (reduced from-to)	100 to 17	70 to 13	50 to 13	40 to 12	30 to 11	20 to 8
	Recognition Rate					
Linear	76.02%	73.10%	71.35%	70.76%	68.4%	59.1%
Polynomial 2 nd	44.44%	70.76%	71.35%	70.18%	72.51%	70.18%
KNN:1	81.29%	80.12%	81.29%	80.12%	79.53%	76.61%
KNN:3	77.19%	75.44%	73.68%	73.10%	71.35%	73.68%
KNN:5	73.68%	73.10%	71.35%	72.51%	70.76%	70.76%
NN network (5 neurons)	80.12%	78.95%	76.61%	76.02%	77.19%	75.44%
NN network (10 neurons)	76.02%	81.29%	80.12%	81.29%	79.53%	76.61%
NN network (15 neurons)	76.61%	79.53%	78.95%	77.19%	75.44%	76.61%
NN network (20 neurons)	80.12%	81.29%	81.87%	78.95%	76.61%	77.19%
NN network (25 neurons)	81.29%	82.46%	81.29%	80.12%	79.53%	78.95%
NN network (30 neurons)	81.87%	82.46%	81.29%	80.12%	79.53%	78.95%
NN network (40 neurons)	82.46%	83.63%	81.87%	82.46%	78.95%	77.19%

4.2 Radon Transform-Based Features

Features such as the shape, area, and distribution of the droplets are captured via horizontal, vertical, and diagonal projections (special cases of the Radon transform) as discussed before. To further compress the resulting Radon coefficients, a one dimensional DCT is applied. From Figures 27 and 28, it can be noticed that the first 30 DCT coefficients possess most of the energy from the DCT vector; hence, these coefficients are adopted as the representative feature vector. Table 9 compares

the results of various classifiers using the first 30 DCT coefficients of the horizontal, vertical, and diagonal projections of the images. The results in Table 9 suggest that the three projections yield more or less to the same amount of information. This is expected for the kind of images that we are using.

Table 9. X-axis, Y-axis and Diagonal Projection Recognition Rates

Projection angle / Classifier	Linear	2 nd ord Polynomial	KNN (Best of 1,3, & 5 Ks)	ANN (25 Neurons)
0° Degree	68.41%	Rank deficient	73.68%	71.18%
90° Degree	68.41%	Rank deficient	73.68%	73.71%
45° Degree	68.88%	Rank deficient	73.71%	73.10%

The KNN and ANN classifiers performed the best with a 73.71% recognition rate while the 2nd order polynomial classifier suggests the need for a dimensionality reduction technique. Table 10 shows the recognition results using the three aforementioned projections after the application of a stepwise regression.

Table 10. Radon Transform FV Comparison Results after Stepwise Regression

Projection angle / Classifier	Linear	2 nd ord Polynomial	KNN (Best of 1,3, & 5 Ks)	ANN (25 Neurons)
0° Degree	62.71%	77.53%	70.76%	73.77%
90° Degree	62.71%	77.53%	70.76%	72.03%
45° Degree	63.27%	77.19%	71.24%	74.10%

The polynomial classifier now shows the best recognition rate of 77.53% after the application of the stepwise regression. This confirms the ability of the polynomial classifier to handle nonlinear feature spaces effectively as discussed in the previous

chapter. The stepwise regression has reduced the length of the FV from 30 to 15, thus leading to the stability of the polynomial classifier.

4.3 Wavelet Transform-Based Features

A correlation between the HC images' frequency contents and the classes of samples can be noticed from the previous two sections. The discrete wavelet transform (DWT) allows us to analyze the HC images in different scales. Accordingly, several textural and statistical features can be extracted from these scales. Based on the decomposition level, the wavelet transform will have an "approximation" band and several "details" bands as previously discussed. Textural and statistical features can be extracted from each band to form the FV as shown in Figures 30 and 31. Table 11 shows the classification rates using the extracted statistical features (entropy, energy, and variance) from a four-level Haar wavelet transform. The textural features are extracted using the GLCM algorithm and demonstrated later in Section 4.4.

Table 11. Wavelet-Based Features' Recognition Rates

Classifier / Features	Entropy	Energy	Variance	Entropy +Variance	Energy +Variance	All
Linear	76.02%	64.3%	67.3%	87.13%	84.80%	85.96%
Polynomial 2 nd	70.18%	71.93%	71.93%	Rank deficient	Rank deficient	Rank deficient
KNN:1	78.95%	87.72%	81.29%	81.29%	80.70%	87.55%
KNN:3	77.78%	83.63%	85.38%	85.38%	85.96%	90.64%
KNN:5	77.78%	81.29%	82.46%	82.456%	85.38%	88.30%
NN network (5 neurons)	87.13%	88.89%	89.47%	87.719%	88.30%	89.47%
NN network (10 neurons)	88.30%	85.96%	88.89%	90.643%	90.64%	90.64%
NN network (15 neurons)	90.06%	88.30%	87.13%	88.304%	91.23%	91.81%
NN network (20 neurons)	90.64%	89.47%	88.30%	90.058%	91.23%	89.47%
NN network (25 neurons)	89.47%	87.72%	90.06%	87.719%	90.06%	91.23%

The best recognition rate of 91.81% was obtained using the ANN. To compare the effectiveness of each feature, Table 11 suggests that the energy and the variance features perform well individually, while the entropy features alone score 78.95% using KNN-1 as the classifier. Once again, due to numerical instability, the polynomial classifier achieved lower recognition rates compared to both the ANN and the KNN classifier. To reduce the size of the feature vector, a stepwise regression algorithm is applied and the classifiers are reevaluated as per Table 12. The linear classifier rates slightly dropped after using the stepwise regression while the polynomial classifier recognition rates improved. The ANN achieved the highest classification rate as shown in Table 12.

Table 12. Wavelet-Based Features' Classification Rates after Applying Stepwise Regression

Classifier \ Features	Entropy +Variance	Energy +Variance	All
Linear	72.51%	74.85%	80.70%
Polynomial 2 nd	80.702%	85.38%	78.36%
KNN:3	85.96%	88.3041	87.13%
NN network (15 neurons)	91.228%	90.64%	89.47%

4.4 Contourlet Transform-Based Features

The contourlet transform is a development of the wavelet transform that utilizes a double-filter-banks structure to capture the smoothness among the image contours as detailed in Section 3.1.4. The contourlet transform utilizes a laplacian pyramid filter as demonstrated in Figure 32 to detect singularities and sub-divide the image to an “approximation” and “details” bands depending on the decomposition level. The resulting bands will further pass by the directional filter at a specified array of angles to link the image contours. The extracted features will better estimate the droplets' edges and their intrinsic geometrical structures; this will lead to better extracted features since these characteristics differ across the HC images.

To determine the advantage of the contourlet transform over the wavelet transform, both the statistical and textural analysis of both transforms are compared in Tables 13 and 14, respectively. Both tables present the best features extracted from both transforms after applying the stepwise regression using the best level of decomposition in each method. The best wavelet transform statistical feature recognition rates were obtained using a 4-level Haar wavelet resulting in 13 sub-bands from which the statistical features were extracted. On the other hand, the results from the contourlet transform were obtained using a “pkva” 2-level laplacian pyramid filter and a raised-cosine 1-level directional filter resulting in a 5 sub-band structure from which the statistical features were extracted. The recognition results using the contourlet transform were slightly higher than those obtained using the wavelet transform.

Table 13. Wavelet vs Contourlet Statistical Features.

Classifier Features	Wavelet: Energy +Variance Features	Wavelet: Energy +Entropy +Variance	Contourlet: Energy +Variance Features	Contourlet: Energy +Entropy +Variance
linear	74.85%	80.70%	76.27%	83.12%
Polynomial 2 nd	85.38%	78.36%	88.51%	88.67%
KNN:3	88.3041	87.13%	91.32%	91.13%
NN network (15 neurons)	90.64%	89.47%	91.03%	91.97%

Table 14 demonstrates the recognition results using textural features via an 8x8 GLCM matrix on each sub-band. The recognition results are compared after applying dimensionality reduction using stepwise regression since most of the GLCM matrix coefficients are zeros. The dimensionality is mostly reduced from a 64 coefficient to a maximum of 12 elements in most cases. The best decomposition level to obtain the finest textural analysis on the sub-bands of the wavelet was a 1-level Haar wavelet resulting in a 4 sub-bands compared to the 4-level with 13 sub-bands for the statistical features. Similarly for the contourlet transform, the decomposing level was reduced to

a 1-level laplacian pyramid filter and a 1-level directional filter to acquire the best results.

Table 14. Wavelet vs. Contourlet Textural Features

Classifier Features	Wavelet Textural Analysis: GLCM on Sub-Bands	Contourlet Textural Analysis: GLCM on Sub-Bands
linear	76.41%	78.62%
Polynomial 2 nd	79.11%	88.62%
KNN:3	78.49%	86.05%
NN network (15 neurons)	83.73%	90.58%

This indicates the effectiveness of the GLCM matrix in textural analysis with fewer decomposition levels as it compares the gray level variance of each pixel to its neighbors as detailed previously in Section 3.1.5 and further discussed in the next section.

4.5 GLCM Based-Features

In the previous section, it was noticed that the recognition rate increases significantly as the GLCM matrix was applied on fewer decomposition levels of the wavelet and contourlet transforms. The fact that GLCM is considered as a statistical probability measurement of the gray-level variation between two intensity levels supports its effectiveness for extracting better features when applied to gray-level images directly. This is quite true, especially in this research, as the gray-level variances between the droplets indicate the size of the droplets or wetted areas and even the smoothness of their surfaces. By tuning the appropriate gray levels of the GLCM, the right distance for correlating the neighborhood pixels, and the best direction of the measurement, the GLCM returns what can be considered second-order distinguishing statistical features between the classes under study.

Tables 15-17 demonstrate various GLCM levels and settings to obtain the best FV. Table 15 demonstrates the first comparison to obtain the best GLCM level to

extract the most distinguishing textural features from the HC images. The setting of each GLCM matrix was fixed to a 0^0 direction with a distance of 1 pixel comparison distance to the neighborhood pixels. The results demonstrated in Table 15 suggest that the best decomposition level is an 8x8 GLCM with a recognition rate of 94.15% using the ANN classifier and 92.98% using the KNN. The polynomial classifier performance was acceptable given the fact that all results demonstrated are after the application of the stepwise regression to remove the unrelated coefficients from the GLCM matrix. The 4x4 GLCM matrix size was reduced to 6 after the application of the stepwise regression while the 6x6, 8x8, and 10x10 GLCM matrices were reduced to 7, 10, and 11 coefficients, respectively.

Table 15. Comparison of Various GLCM Levels

Classifier / Features	GLCM-4x4	GLCM-6x6	GLCM-8x8	GLCM-10x10
Linear	88.89%	90.64%	91.2%	91.23%
Polynomial 2 nd	91.81%	91.81%	90.06%	88.9%
KNN:1	91.23%	90.64%	92.40%	91.81%
KNN:3	90.64%	90.06%	90.64%	91.81%
KNN:5	91.81%	89.47%	92.98%	90.64%
NN network (5 neurons)	90.64%	91.81%	90.64%	89.47%
NN network (10 neurons)	89.47%	90.64%	94.15%	88.9%
NN network (15 neurons)	91.81%	90.64%	91.81%	91.23%
NN network (20 neurons)	92.98%	92.98%	94.15%	91.81%
NN network (25 neurons)	91.81%	90.64%	92.98%	92.4%

Table 16 demonstrates the effect of the GLCM directional angle while fixing the decomposition level to 8x8 and the pixel distance to 1. The angle has no significant effect in the textural analysis of the GLCM especially between the x and y axis

directions due to the randomness of the droplet distributions. Table 17 examines the setting of the best choice of pixel distance on an 8x8 GLCM with a zero angle direction. At the beginning, it seemed that the performance of the GLCM increased using the linear and polynomial classifiers when moving from a distance of 1 to 2 pixels. This was related to the reduction of the size of the FV after the stepwise regression as the number of zeros in the GLCM increased as well. The effect of increasing the pixel distance showed its real effect when moving to the third pixel distance as the loss of the interclass distinguishing features came into effect. One of the most significant features in this research is the size of the droplets which is implied in the GLCM textural analysis. Increasing the pixel distance measurement setting has led to increasing the error rate especially between class 1 & 2 where the size difference between the droplets is slight.

Table 16. Comparison of Various GLCM Directional Angles

Classifier / Features	GLCM,8x8, 0 ⁰	GLCM,8x8, 90 ⁰	GLCM,8x8, 45 ⁰
Linear	91.2%	91.2%	91.81%
Polynomial 2 nd	90.06%	90.06%	88.9%
KNN:1	92.40%	92.40%	89.47%
KNN:3	90.64%	90.64%	89.47%
KNN:5	92.98%	92.98%	90.06%
NN network (5 neurons)	90.64%	91.81%	90.64%
NN network (10 neurons)	94.15%	92.98%	92.40%
NN network (15 neurons)	91.81%	90.64%	91.23%
NN network (20 neurons)	94.15%	92.4%	91.81%
NN network (25 neurons)	92.98%	94.15%	92.4%

Other classifiers have a clearer effect on the increase of the pixel distance as their stability is not directly affected by the length of the FV unlike the linear and the polynomial classifiers. Looking at Tables 15-17, the best GLCM level is an 8x8 matrix, with a 1 pixel distance measurement and an angle direction of 0 degrees. The nature of the GLCM is to return several zeros in the output matrix whenever the gray level of the pixel under analysis is not matched within the surrounding pixels. A dimensionality reduction technique such as the stepwise regression which is used in the analysis is quite important as it helps in reducing the unnecessary zeros and coefficients from the matrix and reduces the matrix size significantly from 64 to a maximum of 10 elements in the best case scenario. This procedure reduces the computational cost significantly and helps in the stability of our classifiers especially for the polynomial classifier. The best recognition rate obtained from the GLCM is a 94.15% rate using a 20-neuron ANN classifier.

Table 17. Comparison of the Best GLCM Pixel Neighborhood Distance

Classifier / Features	GLCM,8x8, 0 ⁰ ,d=1	GLCM,8x8, 0 ⁰ , d=2	GLCM,8x8, 0 ⁰ , d=3
Linear	91.2%	91.81%	86.77%
Polynomial 2 nd	90.06%	91.23%	88.9%
KNN:1	92.40%	91.81%	89.47%
KNN:3	90.64%	90.64%	90.64%
KNN:5	92.98%	90.06%	90.06%
NN network (5 neurons)	90.64%	91.81%	88.9%
NN network (10 neurons)	94.15%	89.47%	90.06%
NN network (15 neurons)	91.81%	90.64%	88.9%
NN network (20 neurons)	94.15%	91.81%	91.23%
NN network (25 neurons)	92.98%	91.81%	90.06%

Compared to the other methods, the features extracted from the GLCM have the most distinguishing features. The polynomial classifier also seems to perform well with the reduced dimension FV as the size of the FV is just 10 coefficients and the condition number is 138480. This is not as high as the previous methods, thus indicating the stability of the polynomial classifier. The GLCM matrix analysis is essential to obtain the best FV and its recognition rate could be enhanced to reach a higher rate by fusing other extracted features using some of the previously presented techniques.

4.6 Feature Fusion

Each of the previously presented methods has shown a recognition rate between 70-94% when one class of features was used separately. While some of the extracted features in each method have similarities, some of them perform better in detecting the droplet curves and lines such as the Radon transform and the contourlet transform. Other methods (such as the DCT) have shown the ability to detect the uniformity of the droplet distributions and shapes implied in their frequency contents and their related magnitudes. The statistical features extracted from the wavelet and contourlet transforms have shown inferior recognition rates compared to those obtained by the GLCM matrix since GLCM textural analysis implies second-order statistical features related to the size, shape, and the distribution of the droplets.

In this section, the best features extracted from the presented techniques will be fused (combined) to hopefully a more representative FV. By using a stepwise regression algorithm, the most related features contributing to the classification will be chosen in the construction of the final FV. The fusing will start by the GLCM FV as a base FV while later combining the features from the other methods as demonstrated in Table 18. The best feature combinations obtained from Table 18 were acquired using the GLCM and the Radon transform-based features. An average recognition rate of 95.67% was obtained by fusing the Radon FV with the 8x8 GLCM features as opposed to a rate of 94.15% when using the GLCM features alone. Other combinations have also enhanced the performance of the classifiers indicating an improvement in the distinguishing features extracted. The results of the wavelet and contourlet transform as fused features to the GLCM are similar. This suggests the effectiveness of the directionality factor detected in the GLCM to account for the contourlet advantage over the wavelet. In Table 19, the GLCM + Radon features will

be used as a base FV. Following this, the DCT and the contourlet transform will be fused in order to measure their contribution to the overall recognition rate. The fusing of the contourlet transform with the GLCM + Radon FV shows no improvement of the recognition rates.

Table 18. Feature Fusing with GLCM as a Base FV

Classifier / Features	GLCM + Radon	GLCM +DCT	GLCM +Wavelet	GLCM + Contourlet
Linear	88.89%	91.2%	92.98%	92.98%
Polynomial 2 nd	Rank deficient	Rank deficient	Rank deficient	Rank deficient
KNN:1	95.67%	94.15%	92.40%	92.40%
KNN:3	93.57%	91.81%	90.64%	90.64%
KNN:5	94.15%	93.57%	92.98%	92.98%
NN network (5 neurons)	92.98%	94.15%	92.40%	90.64%
NN network (10 neurons)	95.67%	94.15%	92.40%	92.98%
NN network (15 neurons)	93.57%	91.81%	90.64%	92.40%
NN network (20 neurons)	94.15%	92.98%	90.06%	91.81%
NN network (25 neurons)	92.98%	93.57%	92.98%	94.15%

On the other hand, fusing the DCT FV with the GLCM + Radon FV improved the recognition rate of the KNN to 96.12% and the ANN to 96.51%. To obtain results for the polynomial classifier, the stepwise regression application is modified to obtain a smaller FV. The stepwise regression as a dimensionality reduction technique is applied to the GLCM FV, Radon FV, and the DCT FV separately as a first stage regression as opposed to applying the method directly to the combined FV from the selected methods. The resulting reduced FV from each stage is then fused together and the stepwise regression is applied again to further reduce the size of the final FV to 13 elements. These elements are further expanded using the polynomial to 91

features assuring polynomial stability. The best result of the polynomial classifier was a 93.57% recognition rate which makes it an acceptable choice after the ANN and KNN classifiers.

Table 19. The Effect of DCT and Contourlet Features on the GLCM + Radon FV

Classifier / Features	GLCM + Radon + DCT	GLCM + Radon + Contourlet	All
Linear	90.64%	92.40%	90.64%
Polynomial 2 nd	Rank deficient	Rank deficient	Rank deficient
KNN:1	94.15%	95.67%	94.15%
KNN:3	92.98%	93.57%	92.98%
KNN:5	96.12%	94.15%	96.12%
NN network (5 neurons)	93.57%	93.57%	94.15%
NN network (10 neurons)	95.67%	94.15%	94.15%
NN network (15 neurons)	96.51%	91.81%	93.57%
NN network (20 neurons)	92.98%	94.15%	95.91%
NN network (25 neurons)	93.57%	92.40%	90.64%

4.7 Results Discussion

As seen from the presented results, the GLCM matrix offers the best extracted features and its recognition rate could be further enhanced by fusing other extracted features. In particular, it performs best when fused with DCT and Radon features. The linear classifier results are acceptable in some cases, indicating that the features are mostly linearly separable. However, due to the overlap between the consecutive HC classes, more sophisticated (nonlinear) classifiers are needed. The polynomial classifier has shown a rank deficiency in most of the cases due to the length of the FV, suggesting the need for a dimensionality reduction technique to maintain classifier stability. By using a stepwise regression algorithm, the most related features

contributing to the classification will be chosen in the construction of the final FV which was best demonstrated in the GLCM-based features where the size of the FV was reduced from 64 coefficients to just 10 coefficients. In general, the stepwise regression has the advantage of removing the unrelated or statistically insignificant features from the FV. This procedure enhances the classification mainly in the following ways:

- 1- Reduces the length of the FV dramatically. This has the advantage of reducing the computational cost of the classifiers. It also helps to get out of the dimensionality issue repeatedly encountered with the polynomial classifier.
- 2- Removing the “statistical noise” which includes statistically irrelevant or redundant features. This was found to be very helpful especially in the case of the polynomial classifier.

Although the ANN yields the best performance in the various methods applied, it still has the disadvantage of falling into a local minimum during the training process. Each run of the ANN training produced different recognition rates depending on the random initializing of the algorithm weights. To obtain reliable results, the training of the ANN was performed in a 10 run loop while storing the recognition rate of the resulting 10 networks. The highest recognition rate is then cross checked with another 10 run loops to confirm its repeatability; otherwise the second highest rate will undergo the same procedure until a repetition of the recognition rate is obtained. The resulting trained network is then used to obtain a reliable ANN recognition rate. To investigate the error between the classes, a closer look at the confusion matrix of one of the round Robin runs is demonstrated in Table 20 for the ANN as a classifier and the reduced fusion of GLCM + Radon + DCT as a FV.

In this run, a total of 179 testing samples were classified using the ANN classifier. The resulting errors are 6 samples out of 179 which give a recognition rate of 96.6%. The presented confusion matrix shows few misclassifications between the adjacent HC classes (1&2), (4&5) and only one un-adjacent misclassification between HC2 and HC 4. The errors are focused mainly between class 1 and 2. The slight error between the adjacent classes is acceptable due to the extreme similarity of the images representing these classes. In reality, these might not be true classification errors since they might be due to an original human error during the preparation of the database.

Table 20. Confusion Matrix of One of the Round Robin Runs Using the ANN as a Classifier

	HC1	HC2	HC3	HC4	HC5	HC6	HC7
HC1	20	2	0	0	0	0	0
HC2	1	23	0	1	0	0	0
HC3	0	1	20	0	0	0	0
HC4	0	0	0	20	0	0	0
HC5	0	0	0	1	33	0	0
HC6	0	0	0	0	0	31	0
HC7	0	0	0	0	0	0	26

CHAPTER 5: CONCLUSIONS AND FUTURE WORK:

Silicone rubber insulators (SIR) are currently widely used in transmission lines as an alternative to traditional ceramic insulators due to their advantages in terms of weight, cost, and hydrophobicity. The hydrophobicity of SIRs makes them superior to the traditional ceramic insulators in preventing contamination over their surfaces. However, the main disadvantage of SIR insulators over ceramic ones is ageing due to the existence of organic compounds in their structure. Due to the importance of online monitoring of insulator condition, many utilities around the globe have adopted several effective methods to evaluate insulator surface conditions. Most of these techniques depend on the observation of leakage current (LC) and partial discharge (PD) activities in SIR insulators. Other techniques are more related to monitoring the quality and level of ageing in the rubbery material like the contact angle measurements and hydrophobicity evaluation techniques.

The current hydrophobicity evaluation techniques are subject to the human error. To overcome the human judgment factor, several researchers have suggested the use of digital image processing (DIP) to analyze and measure the contact angle and hence determine the hydrophobicity class (HC) and evaluate the condition of the insulator. Unfortunately there is currently no comprehensive online method to assess the class and condition of the NCI. The attempts to develop an automatic online system based on image processing are limited by various factors including human intervention, localized evaluation, and specific and fixed conditions.

In this research, a discrete cosine transform (DCT), Radon transform, wavelet transform, contourlet transform and gray level co-occurrence matrix (GLCM) have been used to extract textural and statistical distinguishing features to form the final feature vector (FV) to classify the hydrophobicity class. Stepwise regression was used as a method of feature selection and dimensionality reduction. Linear, polynomial, KNN, and ANN classification techniques were used to evaluate the extracted features. The prepared database contains 358 gray-level 481x481 sized images contributing to seven hydrophobicity classes. An effective recognition rate of 96.5% was achieved using combined features based on an 8x8 GLCM at a zero angle and 1 pixel distance measurement, a 40-feature cut-off zigzag transform on a two-dimensional DCT, and a 30-feature DCT cutoff of a Radon transform while using stepwise regression as a

feature selection method and back propagation 15-neuron ANN as a classifier. The proposed system has achieved the purpose of the research which is to automatically assess the condition of SIR insulators. The proposed method is meant to reduce the cost and efforts required by traditional human-based inspection. Even though the proposed system yields very good recognition rates, further improvement can be achieved by acquiring multiple images per observation. For example, using three images per observation can theoretically reduce the misclassification error from 3.5% to 0.1%.

Future work could utilize alternative feature extracting techniques such as the Hough transform and curvelet transform to obtain higher classification rates using smaller FV. Also, the effect of various feature selection and dimensionality reduction techniques such as linear discriminant analysis (LDA) and spectral regression could be further investigated to obtain the best feature selection method. It is also important to study the effect of various factors such as weather conditions and contamination level on the performance of the proposed system.

REFERENCE LIST

- [1]. C. Bayliss and B. Hardy, *Transmission and Distribution Electrical Engineering*, Third Edition, 2007, Elsevier Ltd.
- [2]. I. Jarrar, Feasibility Study: "To implement unmanned aviation vehicles to inspect and scan (infrared) the electrical network (HV Cables, OH Lines, LV systems) and water pipe lines," ASTRO Initiative Cards-Transco 14, October 2011.
- [3]. I.Jarrar, A. El Hag and N. Qaddoumi, "Online techniques to detect defects in Non-Ceramic Insulators (NCI)," *GCC Cigre, Doha, Qatar*, Nov-2010.
- [4]. A. El Hag, "Effect of Insulator Profile on Ageing Performance of Silicone Rubber Insulators", Ph.D. dissertation, Dept. Elect. Eng, Waterloo University, 2003
- [5]. M. S. Naidu and V. Kamaraju, *High Voltage Engineering*, Second Edition, 1995, Tata McGraw-Hill Publishing Ltd.
- [6]. A. El Hag, High Voltage Engineering lecture notes. [On-line], Available: <https://ilearn.aus.edu/webapps/portal/frameset>
- [7]. J.L. Goudie, M. J. Owen, and T. Orbeck. "A review of possible degradation mechanisms of silicone elastomers in high voltage insulation applications." In *Electrical Insulation and Dielectric Phenomena, 1998. Annual Report. Conference on*, vol. 1, pp. 120-127. IEEE, 1998.
- [8]. *High Voltage Silicone Insulators, Electricity Power Technology of the Future*, Elkom-NET ltd, Skopje, Macedonia, Product Catalog, June, 2009.
- [9]. M. Amin and M. Salman, "Ageing of Polymeric Insulators (An Overview)," *Advanced Study Center. Rev.Adv.Mater.Sci. Vol. 13*, pp 93-116, 2006.
- [10]. *Electric Field Computation*, HVEL, High Voltage Engineering Laboratory. [On-line] Retrieved from: http://www.power.uwaterloo.ca/HVEL/Research_Electricfield.htm
- [11]. M. Amin, M. Akbar and S. Amin, "Hydrophobicity of Silicone Rubber Used for Outdoor Insulation (An Overview)", *Advanced Study Center Co. Ltd, Pakistan Taxila, Rev.Adv.Mater.Sci. 16 (2007) 10-26*, 2007
- [12]. S. Gubanski et al, "Tracking on Insulator Surfaces in Presence of Conductive Defects within Housing to Core Interface," *INMR World Congress, Issue 84 Quarter Two 2009 Volume 17 Number 2 Page 74*
- [13]. *Using Infrared Thermography in Utilities*, FLIR. [On-line] Retrieved from: <http://www.flir.com/thermography/eurasia/en/content/?id=11430>

- [14]. I. Jarrar, H. Bashiri, and M. Kuheel, "Partial discharge detection techniques," Department of Electrical Engineering, B.S. design project, American University of Sharjah, UAE, 2008.
- [15]. M. Muhr, R. Schwarz, S. Pack and B. Koerbler, "Unconventional partial discharge measurement," *Annual Report Conference on Electrical Insulation and Dielectric Phenomena*, 2004.
- [16]. STRI Guide: "Composite Insulator Status Program: Field inspection of composite insulators", Guide 3, 98/1, 1998.
- [17]. Z. Linjie et al, "On-line hydrophobicity measurement of composite insulators," School of Electrical Engineering, North China Electric Power University, Beijing, 102206,P.R.China
- [18]. Y. Liu et al, "A New Diagnosis Method on Insulators with Measuring Contact Angles," *International Journal of Intelligent Engineering and Systems, School of Electronic Information, Wuhan University, P.R. China*, Vol.2, No.2,2009.
- [19]. B. X. Du and Yong Liu, "Pattern Analysis of Discharge Characteristics for Hydrophobicity Evaluation of Polymer Insulator," *IEEE Transactions on Dielectrics and Electrical Insulation*, Vol. 18, No. 1; February 2011.
- [20]. M. Berg, R. Thottappillil and V. Scuka, "Hydrophobicity Estimation of HV Polymeric Insulating Materials: Development of a Digital Image Processing Method," *IEEE Transactions on Dielectrics and Electrical Insulation*, Vol. 8 No. 6, December 2001.
- [21]. D. Thomazini, M. V. Gelfuso and R. Altafim, "Hydrophobicity Classification of Polymeric Materials Based on Fractal Dimension," *Materials Research*, Vol. 11, No. 4, 415-419, 2008
- [22]. T. Tokoro, Y. Omoto, Y. Katayama and M. Kosaki, "Image analysis of hydrophobicity and dielectric property of polymer insulating material," *IEEE 2002 Annual Report Conference on Electrical Insulation and Dielectric Phenomena*
- [23]. S. Yi, L. Qin, T. Liangrui and Y. Qiuxia, "A Detection Algorithm of Hydrophobic Levels Based on Triangle Module Operator," Electrical and Electronic Engineering School in North China Electric Power University, Beijing, China.
- [24]. Y. Sun, Q. Li, L. Tang and Q. Yang, "The Fusion Estimating Algorithm of Hydrophobic Level Based on D-S Evidence Theory," School of Electrical and Electronic Engineering, North China Electric Power University, Beijing, China.
- [25]. L. Khalayli, H. Sagban, H. Shoman, K. Assaleh and A. El-Hag, "Automatic Inspection of Outdoor Insulators using Image Processing and Intelligent

Techniques” *the IEEE Electrical Insulation Conference (EIC 2013)*, Ottawa, Canada, June, 2-5, 2013.

- [26]. M. N. Do and Y. M. Lu, “Multidimensional filter banks and multiscale geometric representations,” *Foundations and Trends in Signal Processing*, vol. 5, issue. 3, pp. 157-264, 2012.
- [27]. R. C Gonzalez and R. E. Woods, *Digital Image Processing*, Third Edition, 2008, Prentice Hall.
- [28]. R. C Gonzalez, R. E. Woods and S. L. Eddins, *Digital Image Processing Using Matlab*, Second Edition, 2009, Gatesmark Publishing.
- [29]. MathWorks, Inc. *MATLAB: the language of technical computing. Using MATLAB*. Version. R011b. MathWorks, 2011. *MATLAB Help Documentation: The MathWorks Inc.*, 2011.
- [30]. FINEPIX, JV 200 Series Owner Manual-01. [Online], Retrieved from http://www.fujifilm.com/products/digital_cameras/index.html
- [31]. G. Beliakov, S. James, and L. Troiano, "Texture recognition by using GLCM and various aggregation functions," *Fuzzy Systems, 2008. FUZZ-IEEE 2008. (IEEE World Congress on Computational Intelligence). IEEE International Conference on* , vol., no., pp.1472,1476, 1-6 June 2008
- [32]. T. Shanableh, and K. Assaleh. "Feature modeling using polynomial classifiers and stepwise regression." *Neurocomputing* 73, no. 10 (2010): 1752-1759.
- [33]. R. Ghunem, K. Assaleh, and A. El-Hag, "Artificial neural networks with stepwise regression for predicting transformer oil furan content," *Dielectrics and Electrical Insulation, IEEE Transactions on* ,vol.19, no.2, pp.414,420, April 2012
- [34]. R. Duda, P. Hart, D. Stork, *Pattern Classification*, Second Edition, 2000, John Wiley & Sons, Ltd.
- [35]. A. R. Webb, *Statistical Pattern Recognition*, 2002, Second Edition, John Wiley & Sons, Ltd.
- [36]. D. Paul, E. Bair, T. Hastie and R. Tibshirani, “Preconditioning for feature selection and regression in high dimensional problems,” *The Annals of Statistics*, 2008, Vol. 36, No. 4, 1595–1618
- [37]. K. T. Assaleh, W. M. Campbell, "Speaker identification using a polynomial-based classifier," *Proceedings of the Fifth International Symposium on Signal Processing and Its Applications (ISSPA '99)*, Brisbane, Australia (ISSPA '99), 1999, pp.115-118.

VITA

Ibrahim Marwan Jarrar graduated from Al-Amer High School in the United Arab Emirates (UAE) as class valedictorian in 2004 while maintaining the 5th rank across the UAE's geographical territories (GPA: 99.6%). He received a Regents Scholarship to the American University of Sharjah (AUS), UAE, and was sponsored throughout by the Abu Dhabi Water and Electricity Authority (ADWEA). He graduated magna cum laude in 2008 with a bachelor of science in electrical engineering. He also holds a minor in computer engineering, networking and cyber security. He has also successfully completed the CCNA and CCNB preparation exams. He appeared on the honors list of the School of Engineering throughout his four academic years at AUS and maintained the 4th highest GPA among electrical engineering majors, graduating with a GPA of 3.8 (95%). He started pursuing his master of science degree in AUS in 2010 as a part time student and has successfully fulfilled its requirements with a GPA of 4.0 (100%).

Eng. Ibrahim started working at Abu Dhabi Transmission and Dispatch Company (TRANSCO), a subsidiary company of ADWEA, as an electrical engineer for the Abu Dhabi Maintenance Department since 2008. His main responsibilities include carrying out day-to-day preventive, corrective, and breakdown maintenance activities on electrical systems, plants, and equipment. He is responsible for various electrical systems ranging from 0.4 up to 33 kV that include LV/ HV motors, control systems and circuits, power, shift, cascade and auto transformers, MVSG, LVSG, cables, MV and LV bays, feeders, and ducts, electrical submersible pumps (ESPs), protection systems (OC, EF, REF, Diff, Solkor, Motor, etc), LV and MV electrical variable speed drive systems (EVSDS), battery chargers, DC and UPS, cathodic protection, chlorination systems, hypo chlorite systems, OH cranes and station auxiliary services.

Eng. Ibrahim's current interests include condition monitoring, testing, and diagnostics of HV insulation and electrical equipment. He has successfully carried out research in this area and has participated in several conferences organized by IEEE, CIGRE, SPE, and IPTC.